IEEE Access
Multidisciplinary ⋮ Rapid Review ⋮ Open Access Journal

Received June 12, 2019, accepted July 4, 2019, date of publication July 22, 2019, date of current version August 6, 2019.

Digital Object Identifier 10.1109/ACCESS.2019.2930201

Tightly-Coupled Monocular Visual-Odometric SLAM Using Wheels and a MEMS Gyroscope

MEIXIANG QUAN[1], SONGHAO PIAO[1], MINGLANG TAN[2], AND SHI-SHENG HUANG[2]
[1]School of Computer Science and Technology, Harbin Institute of Technology, Harbin 150001, China
[2]Hyperception, Inc., Beijing 100083, China

Corresponding authors: Songhao Piao (piaosh@hit.edu.cn) and Shi-Sheng Huang (shishenghuang.net@gmail.com)

This work was supported in part by the National Science Foundation of China under Grant 61375081, and in part by the Special Fund Project of Harbin Science and Technology Innovation Talents Research under Grant RC2013XK010002.

ABSTRACT In this paper, we present a novel tightly coupled probabilistic monocular visual-odometric simultaneous localization and mapping (VOSLAM) algorithm using wheels and a MEMS gyroscope, which can provide accurate, robust, and long-term localization for ground robots. First, we present a novel odometer preintegration theory on manifold; it integrates the wheel encoder measurements and gyroscope measurements to a relative motion constraint that is independent of the linearization point and carefully addresses the uncertainty propagation and gyroscope bias correction. Based on the preintegrated odometer measurement model, we also introduce the odometer error term and tightly integrate it into the visual optimization framework. Then, in order to bootstrap the VOSLAM system, we propose a simple map initialization method. Finally, we present a complete localization mechanism to maximally exploit both sensing cues, which provides different strategies for motion tracking when: 1) both measurements are available; 2) visual measurements are not available; and 3) wheel encoders experience slippage, thereby ensuring the accurate and robust motion tracking. The proposed algorithm is evaluated by performing extensive experiments, and the experimental results demonstrate the superiority of the proposed system.

INDEX TERMS Motion estimation, sensor fusion, simultaneous localization and mapping.

I. INTRODUCTION

Simultaneous localization and mapping (SLAM) from onboard sensors is a fundamental and key technology for autonomous mobile robot to safely interact within its workspace. SLAM is a technique that builds a globally consistent representation of the environment (i.e. the map) and estimates the state of robot in the map simultaneously. Because SLAM can be used in many practical applications, such as autonomous driving, indoor service robots, and virtual or augmented reality, it has received considerable attention from Robotics and Computer Vision communities.

In this paper, we study the monocular vision-based localization and mapping algorithm for domestic ground robots moving on a plane, such as cleaning robot, nursing robot, and restaurant robot waiter. When localizing the domestic ground robots, planar-motion constraint is often used to improve the localization accuracy. There are two ways to use planar-motion constraint. One is deterministic planar-motion constraint, in which the constraint is not affected by noise, i.e., the robot is thought to move on a deterministic plane. The other is stochastic planar-motion constraint, in which the constraint is affected by Gaussian noise, thereby taking into account the out-of-plane motion perturbations. Some visual SLAM (VSLAM) system for ground robots have parameterized the pose as SE(2), i.e., deterministic planar-motion constraint, to only consider the deterministic in-plane motion, e.g. in [1]. However in practical environment, ground robots are moving on an approximately flat surface due to the uneven terrains, some objects on the ground, and vibrations of the moving platform. When the robot motion is often out of the constrained planar model, since visual observation is highly coupled with all 6 DoF of 3D pose, the deterministic planar-motion constraint will result to decrease in visual localization accuracy. Thereby as in [2], we parameterize the pose as SE(3) and add a stochastic planar-motion constraint on the pose, which can explicitly model the approximately in-plane motion of the robot.

For localizing the robot in indoor environment, monocular visual-inertial setup is the minimum and most commonly

The associate editor coordinating the review of this manuscript and approving it for publication was Chao Tan.

used sensor suite due to the complementary characteristics of both sensors. Monocular visual-inertial SLAM (VISLAM) system [3]–[6] can accurately localize the sensor with general 3D motion. However, ground robots interested in this paper are usually constrained to move along straight lines or circular arcs with constant acceleration. As demonstrated in [2], when the robot moves with these specific motions, the monocular VISLAM has additional unobservable directions, e.g. scale, which causes the significant estimation error. Therefore, monocular visual-inertial sensor suite is not able to provide accurate motion tracking for ground robots.

Most ground robots are equipped with wheel encoders. In most cases, wheel encoders provide the reliable inter-frame traveled distance measurements of each wheel at low frequency. Traditional monocular visual-odometric SLAM (VOSLAM) methods [7], [8] just use distance information from wheel encoders to render the scale factor observable, which is due to the fact that the wheel encoders even provide poor orientation estimation for planar trajectory as demonstrated in [8]. Even though the wheel encoders can provide accurate in-plane rotation, when the robot motion is often out of the plane constraint, the encoders can only provide the accurate traveled distance, not the accurate relative transformation. In contrast, the MEMS gyroscope provides accurate inter-frame rotational information at high frequency. Therefore in this paper, we fuse distance measurements from wheel encoders with angular velocity measurements from gyroscope to provide an accurate inter-frame SE(3) relative transformation for both in-plane motion and out-of-plane motion. In the following, we will call the wheel encoders and MEMS gyroscope as odometer. Then by fusing the odometer measurements with visual measurements, we construct a novel tightly-coupled optimization-based monocular VOSLAM system.

The contributions of the paper are as follows. In order to tightly and efficiently integrate the odometer measurements to VSLAM system in the framework of nonlinear optimization, it is important to provide the integrated odometer measurements between the selected keyframes. Motivated by the inertial measurement unit (IMU) preintegration theory proposed in [9], we present a novel odometer preintegration theory on manifold. The preintegration theory integrates the measurements from odometer to a single relative motion constraint that is independent of the change of linearization point, thereby eliminating the repeated computation. Besides, we also derive the corresponding uncertainty propagation and bias correction theory. Then based on the proposed preintegrated odometer measurement model, we formulate a preintegrated odometer factor and tightly integrate it to the visual-odometric optimization framework.

Secondly, since the proposed VOSLAM system requires a good initial value to bootstrap, we present a simple initialization method that builds an initial map of the environment with scale and selectively estimates the initial value of gyroscope bias. Finally, since both visual and odometer measurements are not always available, we present a complete visual-odometric tracking mechanism to maximally exploit both measurement information. For the situation where both measurements are available, we tightly fuse both measurements to provide the accurate motion tracking. For the situation where visual information is not available, we use odometer measurements to improve the robustness of our system, and we also offer some strategies to render the visual information available as soon as possible. In addition, for the situation where wheel encoders experience slippage, we provide a strategy to detect and compensate for the faulty measurement. In this way, we can track the motion of ground robots accurately and robustly.

In experiments, we carry out extensive experiments to demonstrate the superior accuracy and robustness of our algorithm.

An overview of the proposed algorithm is shown in Fig. 1. The remainder of this article is organized as follows. Section II discusses relevant literature. In Section III, we introduce the preliminaries of the paper. Preintegrated odometer measurements and tightly-coupled visual-odometric nonlinear optimization on manifold are introduced in Section IV. In Section V, the complete monocular VOSLAM system is discussed. The experimental results are shown in Section VI. Finally, Section VII concludes the paper.

II. RELATED WORK

There are extensive scholarly works on monocular visual odometry (VO) and VSLAM, these works rely on either filtering methods or nonlinear optimization methods. Filtering based approaches achieve higher computational efficiency due to the continuous marginalization of past state. The first real-time monocular VSLAM - MonoSLAM [10] is an extended kalman filter (EKF) based method. The standard way of computing Jacobian by filtering methods leads the system to have incorrect observability, which results in inconsistency and slightly lower accuracy. To solve this problem, the first-estimates Jacobian approach was proposed in [11]. The method computed Jacobian with the first-ever available estimate instead of different linearization points, which makes the system observability correct and thereby improves the consistency and accuracy of the system. In addition, the observability-constrained EKF [12] was proposed to explicitly enforce the unobservable directions of the system, hence improving its consistency and accuracy.

On the other hand, nonlinear optimization based approaches can better deal with the nonlinearity of system due to its ability to re-linearize measurement models, thereby achieving better accuracy at the expense of high computational cost. The first real-time optimization based monocular VSLAM system is PTAM [13] proposed by Klein and Murray. The method achieved real-time performance by dividing the SLAM system into two parallel threads. In one thread, the system performs bundle adjustment over selected keyframes and constructs map points to obtain accurate map of the environment. In the other parallel thread,

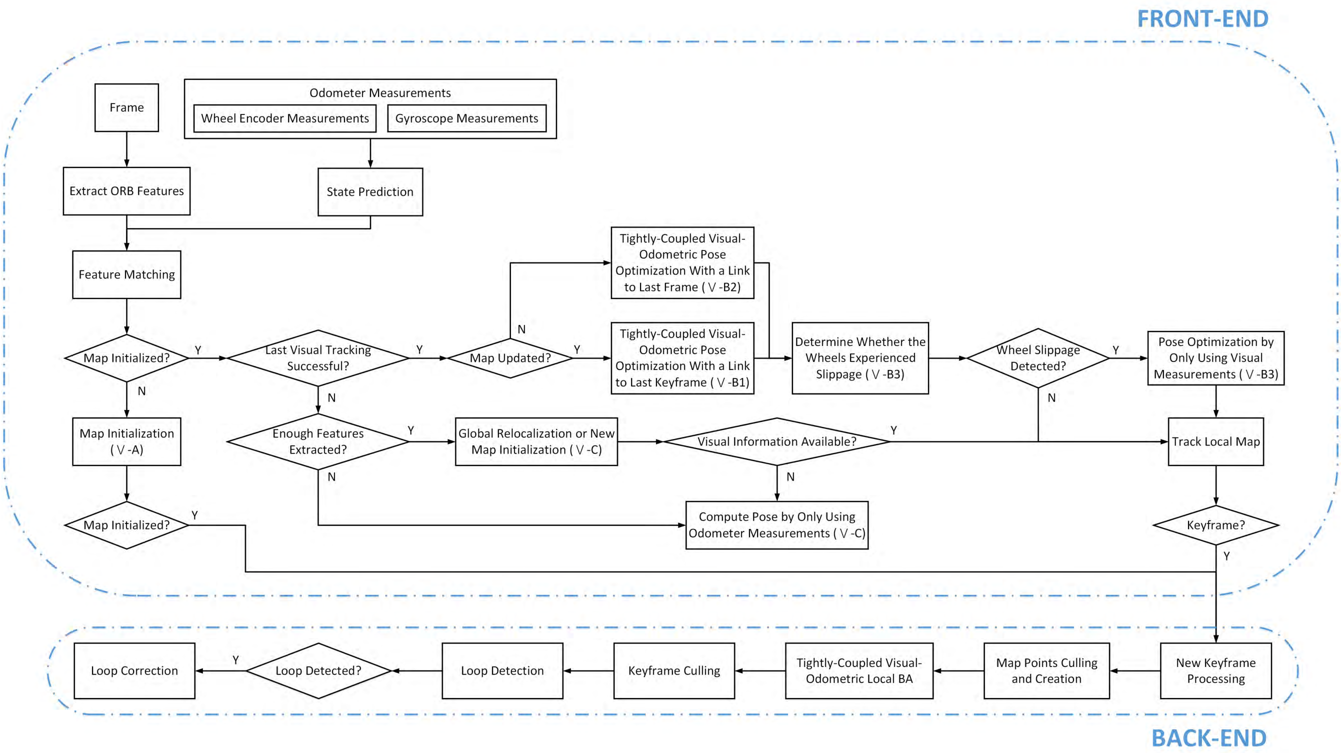
FRONT-END
Frame
Odometer Measurements
Wheel Encoder Measurements
Gyroscope Measurements
Extract ORB Features
State Prediction
Feature Matching
Tightly-Coupled Visual-Odometric Pose Optimization With a Link to Last Frame (V-B2)
N
Map Initialized?
Y
Last Visual Tracking Successful?
Y
Map Updated?
Y
Tightly-Coupled Visual-Odometric Pose Optimization With a Link to Last Keyframe (V-B1)
Determine Whether the Wheels Experienced Slippage (V-B3)
Wheel Slippage Detected?
Y
Pose Optimization by Only Using Visual Measurements (V-B3)
N
N
N
Map Initialization (V-A)
Enough Features Extracted?
Y
Global Relocalization or New Map Initialization (V-C)
Visual Information Available?
Y
Track Local Map
N
N
Map Initialized?
Y
Compute Pose by Only Using Odometer Measurements (V-C)
Keyframe?
Y
Loop Correction
Y
Loop Detected?
Loop Detection
Keyframe Culling
Tightly-Coupled Visual-Odometric Local BA
Map Points Culling and Creation
New Keyframe Processing
BACK-END

FIGURE 1. A flow chart illustrating the full pipeline of the proposed system.

the camera pose is tracked by minimizing the reprojection error of features that match the reconstructed map points. Based on the work of PTAM, a versatile monocular VSLAM system ORB-SLAM [14] was presented. The system introduced the third loop closing thread to eliminate the accumulated error when revisiting an already reconstructed area, which is achieved by taking advantage of bag-of-words [15] and 7 degree-of-freedom (dof) pose graph optimization [16].

In addition, according to the definition of visual residual model, monocular VSLAM can also be categorized into feature based approaches and direct approaches. The above mentioned methods are all feature based approaches, which is quite mature and able to provide accurate estimate. However, the approaches fail to track in poorly textured environments and need to consume extra computational resources to extract and match features. In contrary, direct approaches work on raw sensor measurements, which makes the methods more efficient and able to exploit image information where gradient is small. Therefore, direct methods can outperform feature based methods in low texture environment. DTAM [17], SVO [18], LSD-SLAM [19], and DSO [20] are direct monocular VSLAM systems, which builds a dense or semi-dense map from monocular images in real-time, however their accuracy is still lower than the feature based semi-dense mapping technique [21].

The monocular VSLAM is scale ambiguous and sensitive to motion blur, occlusions, and illumination changes. Therefore, the monocular VSLAM systems are often combined with other odometric sensors, especially IMU sensor, to achieve accurate and robust tracking system. Tightly-coupled VISLAM can also be categorized into filtering based methods and optimization based methods, where visual and inertial measurements are fused from the raw measurement level. Papers [3], [22]–[25] are filtering based monocular VISLAM approaches, which uses the inertial measurements to accurately predict the motion movement between two consecutive frames. An elegant example for filtering based visual-inertial odometry (VIO) system is MSCKF [3], it can achieve high-precision motion estimation with computational complexity only linear in the number of features, which is achieved by presenting a visual measurement model that excludes point features from the state vector.

OKVIS [4] is an optimization based monocular VISLAM system, which tightly integrates the inertial measurements in a keyframe-based visual-inertial pipeline under the framework of graph optimization. However in this system, the IMU integration needs to be computed repeatedly whenever the linearization point changes. In order to eliminate this repeated computation, Forster *et al.* presented an IMU preintegration theory, and tightly integrated the preintegrated IMU factor and the visual factor in a fully probabilistic manner in [9]. Later, a new tightly-coupled monocular VISLAM system - ORB-VISLAM [5] was presented. The system can close loop and reuse the previously estimated 3D map, thereby achieving higher accuracy and robustness. Recently, another tightly-coupled monocular VISLAM system was proposed in [6], [26], which provides accurate and robust motion tracking by performing local bundle adjustment (BA) for each frame and its capability to close loop.

There are also several works on the monocular VOSLAM that fuses visual measurements with wheel encoder measurements. In [7], [8], distance information from wheel encoders was fused with visual measurements to render the scale factor observable, which is performed in the framework of optimization. In [27], wheel encoder measurements were integrated to the visual odometry system for accurate motion prediction, thus true scale of the system can be recovered. In addition, the author of [2] proved that for the ground robot that moves along straight lines or circular arcs with constant acceleration, monocular VIO/VISLAM has additional unobservable directions, e.g. scale. Therefore, they integrated the wheel encoder measurements with VIO system in a tightly-coupled manner to render the scale of the system observable.

III. PRELIMINARIES

We begin by briefly defining the notations used throughout the paper. We employ $(\cdot)^W$ to denote the world reference frame, $(\cdot)^{O_k}$, $(\cdot)^{C_k}$ and $(\cdot)^{B_k}$ to denote the wheel frame, camera frame and inertial frame for the k^{th} image. In the following, we employ $\mathbf{R}_{\mathcal{F}_2}^{\mathcal{F}_1} \in \mathbf{SO}(3)$ to represent rotation from frame $\{\mathcal{F}_2\}$ to $\{\mathcal{F}_1\}$ and $\mathbf{p}_{\mathcal{F}_2}^{\mathcal{F}_1} \in \mathbb{R}^3$ to describe the 3D position of frame $\{\mathcal{F}_2\}$ with respect to frame $\{\mathcal{F}_1\}$. Besides, we use $\mathbf{I}_{n\times n}$ to denote $n \times n$ identity matrix and $\mathbf{0}_{n\times m}$ to denote $n \times m$ zero matrix.

The rotation and translation between rigidly mounted wheel and camera sensor are $\mathbf{R}_O^C \in \mathbf{SO}(3)$ and $\mathbf{p}_O^C \in \mathbb{R}^3$ respectively, and $\mathbf{R}_B^O \in \mathbf{SO}(3)$ denotes the rotation from inertial frame to wheel frame, these parameters can be obtained from calibration. In addition, the rigid-body transformation $\mathbf{T}_W^{O_k} = \begin{bmatrix} \mathbf{R}_W^{O_k} & \mathbf{p}_W^{O_k} \\ \mathbf{0}^T & 1 \end{bmatrix} \in \mathbf{SE}(3)$ denotes the pose of the k^{th} image, and the 3D position of the j^{th} map point in global frame $\{W\}$ and camera frame $\{C_k\}$ are denoted as $\mathbf{f}_j^W \in \mathbb{R}^3$ and $\mathbf{f}_j^{C_k} \in \mathbb{R}^3$ respectively.

In order to provide a minimal representation for the rigid-body transformation during the optimization, we use a vector $\boldsymbol{\xi} \in \mathbb{R}^3$ computed from the Lie algebra of $\mathbf{SO}(3)$ to represent the over-parameterized rotation matrix $\mathbf{R}$. The Lie algebra of $\mathbf{SO}(3)$ is denoted as $\mathfrak{so}(3)$, which is the tangent space of manifold and coincides with the space of 3×3 skew symmetric matrices. The logarithm map associates a rotation matrix $\mathbf{R} \in \mathbf{SO}(3)$ to a skew symmetric matrix:

$$\boldsymbol{\xi}^\wedge = \log(\mathbf{R}) \tag{1}$$

where $(\cdot)^\wedge$ operator maps a 3-dimensional vector to a skew symmetric matrix, thus the vector $\boldsymbol{\xi}$ can be computed by using inverse $(\cdot)^\vee$ operator:

$$\boldsymbol{\xi} = \mathrm{Log}(\mathbf{R}) = \log(\mathbf{R})^\vee \tag{2}$$

Inversely, the exponential map associates the Lie algebra $\mathfrak{so}(3)$ to the rotation matrix $\mathbf{R} \in \mathbf{SO}(3)$:

$$\mathbf{R} = \mathrm{Exp}(\boldsymbol{\xi}) = \exp(\boldsymbol{\xi}^\wedge) \tag{3}$$

The input of our estimation problem is a stream of measurements from the monocular camera and the odometer. The visual measurement is a set of point features extracted from the captured intensity image $\mathrm{I}_k : \Omega \subset \mathbb{R}^2 \to \mathbb{R}$ at time-step k. Such measurement is obtained by camera projection model $\pi : \mathbb{R}^3 \to \mathbb{R}^2$, which projects the l^{th} map point $\mathbf{f}_l^{C_k} = (x_c, y_c, z_c)^\mathrm{T} \in \mathbb{R}^3$ expressed in the current camera frame onto the image coordinate $\mathbf{z}_{kl} = (u, v)^\mathrm{T} \in \Omega$:

$$\begin{aligned} \widetilde{\mathbf{z}}_{kl} &= \mathbf{z}_{kl} + \boldsymbol{\sigma}_{kl} \\ &= \pi(\mathbf{f}_l^{C_k}) + \boldsymbol{\sigma}_{kl} \end{aligned} \tag{4}$$

where $\widetilde{\mathbf{z}}_{kl}$ is the corresponding feature measurement, and $\boldsymbol{\sigma}_{kl}$ is the 2×1 measurement noise with covariance $\boldsymbol{\Sigma}_{C_{kl}}$. The projection function π is determined by the intrinsic parameters of camera, which is known from calibration.

In addition, the gyroscope of odometer provides the angular velocity measurement $\widetilde{\boldsymbol{\omega}}_k$ at time-step k, the measurement is assumed to be affected by a slowly time-varying bias $\mathbf{b}_{g_k}$ and a discrete-time zero-mean Gaussian white noise $\boldsymbol{\eta}_{gd} \sim \mathcal{N}(\mathbf{0}, \boldsymbol{\Sigma}_{gd})$:

$$\widetilde{\boldsymbol{\omega}}_k = \boldsymbol{\omega}_k + \mathbf{b}_{g_k} + \boldsymbol{\eta}_{gd} \tag{5}$$

where gyroscope bias $\mathbf{b}_{g_k}$ is modeled as random walk, hence its derivative is Gaussian noise $\boldsymbol{\eta}_{b_g} \sim \mathcal{N}(\mathbf{0}, \boldsymbol{\Sigma}_{b_g})$:

$$\dot{\mathbf{b}}_{g_k} = \boldsymbol{\eta}_{b_g} \tag{6}$$

The wheel encoders of odometer measure the traveled distance $\widetilde{\mathrm{Dl}}_k$ and $\widetilde{\mathrm{Dr}}_k$ of both wheels from time-step $k-1$ to k at time-step k, which is assumed to be affected by a discrete-time zero-mean Gaussian white noise η_{ed} with variance σ_{ed}:

$$\begin{aligned} \widetilde{\mathrm{Dl}}_k &= \mathrm{Dl}_k + \eta_{ed} \\ \widetilde{\mathrm{Dr}}_k &= \mathrm{Dr}_k + \eta_{ed} \end{aligned} \tag{7}$$

Therefore, the 3D position of frame $\{O_k\}$ with respect to frame $\{O_{k-1}\}$ measured by wheel encoders is $\widetilde{\boldsymbol{\psi}}_{O_k}^{O_{k-1}} = \begin{bmatrix} \dfrac{\widetilde{\mathrm{Dl}}_k + \widetilde{\mathrm{Dr}}_k}{2} & 0 & 0 \end{bmatrix}^\mathrm{T}$, which is affected by a Gaussian noise $\boldsymbol{\eta}_{\psi d} \sim \mathcal{N}(\mathbf{0}, \boldsymbol{\Sigma}_{\psi d})$:

$$\begin{aligned} \widetilde{\boldsymbol{\psi}}_{O_k}^{O_{k-1}} &= \boldsymbol{\psi}_{O_k}^{O_{k-1}} + \boldsymbol{\eta}_{\psi d} \\ &= -\mathbf{R}_W^{O_{k-1}} \mathbf{R}_W^{O_k\,\mathrm{T}} \mathbf{p}_W^{O_k} + \mathbf{p}_W^{O_{k-1}} + \boldsymbol{\eta}_{\psi d} \end{aligned} \tag{8}$$

where $\mathbf{R}_W^{O_{k-1}}$ and $\mathbf{p}_W^{O_{k-1}}$ constitute the pose of frame $\{O_{k-1}\}$, and $\mathbf{R}_W^{O_k}$ and $\mathbf{p}_W^{O_k}$ constitute the pose of frame $\{O_k\}$. In addition, the covariance of noise $\boldsymbol{\eta}_{\psi d}$ is computed from the 1-dimensional noise η_{ed} with $\boldsymbol{\Sigma}_{\psi d} = \frac{\sigma_{ed}}{2}\mathbf{I}_{3\times 3}$.

In many cases, the ground robot is moving on an approximately planar surface. The motion on a plane has 3 DoF in contrast to 6DoF of 3D motion. The additional information can improve the accuracy of system. Therefore for each

SE(3) pose, we also provide a planar measurement $\widetilde{\mathbf{pl}}_k = [0, 0, 0]^{\mathrm{T}} \in \mathbb{R}^3$ with noise $\boldsymbol{\eta}_{pl} \sim \mathcal{N}(\mathbf{0}, \boldsymbol{\Sigma}_{\mathrm{pl}})$ to constrain its roll, pitch angles and z-axis translation with respect to the physical plane.

IV. TIGHTLY-COUPLED VISUAL-ODOMETRIC NONLINEAR OPTIMIZATION ON MANIFOLD

We use $\mathcal{K}$ to denote a set of successive keyframes from i to j, and $\mathcal{L}$ to denote all the landmarks visible from the keyframes in $\mathcal{K}$. Then the variables to be estimated in the window of keyframes from i to j is:

$$\boldsymbol{\mathcal{X}} = \{\boldsymbol{x}_k, \mathbf{f}_l^W\}_{k\in\mathcal{K}, l\in\mathcal{L}} \tag{9}$$

where $\boldsymbol{x}_k = \{\mathbf{T}_W^{O_k}, \mathbf{b}_{g_k}\}$ is the state of keyframe k.

We denote the visual measurements of $\mathcal{L}$ at keyframe i as $\boldsymbol{\mathcal{Z}}_{C_i} = \{\widetilde{\mathbf{z}}_{il}\}_{l\in\mathcal{L}}$. In addition, we denote the odometer measurements between two consecutive keyframes i and j as $\boldsymbol{\mathcal{O}}_{ij} = \{\widetilde{\boldsymbol{\omega}}_t, \widetilde{\mathrm{Dl}}_t, \widetilde{\mathrm{Dr}}_t\}_{t_i\leq t\leq t_j}$. Therefore, the set of measurements collected for optimizing the state $\boldsymbol{\mathcal{X}}$ is:

$$\boldsymbol{\mathcal{Z}} = \{\boldsymbol{\mathcal{Z}}_{C_i}, \boldsymbol{\mathcal{O}}_{ij}, \widetilde{\mathbf{pl}}_i\}_{(i,j)\in\mathcal{K}} \tag{10}$$

A. MAXIMUM A POSTERIORI ESTIMATION

The optimum value of state $\boldsymbol{\mathcal{X}}$ is estimated by solving the following maximum a posteriori (MAP) problem:

$$\boldsymbol{\mathcal{X}}^* = \underset{\boldsymbol{\mathcal{X}}}{\mathrm{argmax}}\ p\left(\boldsymbol{\mathcal{X}}|\boldsymbol{\mathcal{Z}}\right) \tag{11}$$

which means that given the available measurements $\boldsymbol{\mathcal{Z}}$, we want to find the best estimate for state $\boldsymbol{\mathcal{X}}$. Assuming measurements $\boldsymbol{\mathcal{Z}}$ are independent, then using Bayes' rule, we can rewrite $p\left(\boldsymbol{\mathcal{X}}|\boldsymbol{\mathcal{Z}}\right)$ as:

$$\begin{aligned} &p(\boldsymbol{\mathcal{X}}|\boldsymbol{\mathcal{Z}}) \\ &\ \propto p(\boldsymbol{\mathcal{X}}_0)\, p(\boldsymbol{\mathcal{Z}}|\boldsymbol{\mathcal{X}}) \\ &\ = p(\boldsymbol{\mathcal{X}}_0) \prod_{(i,j)\in\mathcal{K}} p(\boldsymbol{\mathcal{Z}}_{C_i},\ \boldsymbol{\mathcal{O}}_{ij},\ \widetilde{\mathbf{pl}}_i|\boldsymbol{\mathcal{X}}) \\ &\ = p(\boldsymbol{\mathcal{X}}_0) \prod_{(i,j)\in\mathcal{K}} p(\boldsymbol{\mathcal{O}}_{ij}|\boldsymbol{x}_i, \boldsymbol{x}_j) \prod_{i\in\mathcal{K}} \prod_{l\in\mathcal{L}} p(\widetilde{\mathbf{z}}_{il}|\boldsymbol{x}_i, \mathbf{f}_l^W) \prod_{i\in\mathcal{K}} p(\widetilde{\mathbf{pl}}_i|\boldsymbol{x}_i) \end{aligned} \tag{12}$$

The equation can be interpreted as a factor graph. The variables in $\boldsymbol{\mathcal{X}}$ are corresponding to nodes in the factor graph. The terms $p(\boldsymbol{\mathcal{X}}_0)$, $p(\boldsymbol{\mathcal{O}}_{ij}|\boldsymbol{x}_i, \boldsymbol{x}_j)$, $p(\widetilde{\mathbf{z}}_{il}|\boldsymbol{x}_i, \mathbf{f}_l^W)$, and $p(\widetilde{\mathbf{pl}}_i|\boldsymbol{x}_i)$ are called factors, which encodes probabilistic constraints between nodes. A factor graph representing the problem is shown in Fig. 2.

The MAP estimate corresponds to the minimum of the negative log-posterior. Under the assumption of zero-mean Gaussian noise, the MAP estimate in (11) can be written as the minimum of the sum of squared residual errors:

$$\begin{aligned} \boldsymbol{\mathcal{X}}^* &= \underset{\boldsymbol{\mathcal{X}}}{\mathrm{argmin}} -\log p(\boldsymbol{\mathcal{X}}|\boldsymbol{\mathcal{Z}}) \\ &= \underset{\boldsymbol{\mathcal{X}}}{\mathrm{argmin}} \|\mathbf{r}_0\|^2_{\boldsymbol{\Sigma}_0} + \sum_{(i,j)\in\mathcal{K}} \rho\left(\|\mathbf{r}_{\mathcal{O}_{ij}}\|^2_{\boldsymbol{\Sigma}_{\mathcal{O}_{ij}}}\right) \\ &\quad + \sum_{i\in\mathcal{K}} \sum_{l\in\mathcal{L}} \rho\left(\|\mathbf{r}_{\mathcal{C}_{il}}\|^2_{\boldsymbol{\Sigma}_{\mathcal{C}_{il}}}\right) + \sum_{i\in\mathcal{K}} \rho\left(\|\mathbf{r}_{\mathrm{pl}_i}\|^2_{\boldsymbol{\Sigma}_{\mathrm{pl}}}\right) \end{aligned} \tag{13}$$

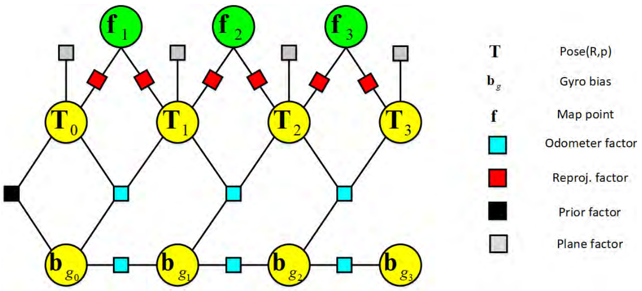

FIGURE 2. Factor graph representing the visual-odometric optimization problem. The states are shown as circles and factors are shown as squares. The blue squares represent the odometer factors and connect to the state of last keyframe, red squares denote the visual factors, black squares denote the prior factors, and gray squares denote the plane factors.

where $\mathbf{r}_0$, $\mathbf{r}_{\mathcal{O}_{ij}}$, $\mathbf{r}_{\mathcal{C}_{il}}$, and $\mathbf{r}_{\mathrm{pl}_i}$ are the prior error, odometer error, reprojection error, and plane error respectively, as well as $\boldsymbol{\Sigma}_0$, $\boldsymbol{\Sigma}_{\mathcal{O}_{ij}}$, $\boldsymbol{\Sigma}_{\mathcal{C}_{il}}$, and $\boldsymbol{\Sigma}_{\mathrm{pl}}$ are the corresponding covariance matrices, and ρ is the Huber robust cost function. In the following subsections, we provide the detailed expressions for these residual errors.

B. PREINTEGRATED ODOMETER MEASUREMENTS

In this section, we derive the preintegrated odometer measurement between two consecutive keyframes i and j by assuming the gyroscope bias of keyframe i is known. Firstly, we define the rotation increment $\Delta\mathbf{R}_{ij}$ and position increment $\Delta\mathbf{p}_{ij}$ in frame $\{O_i\}$ as:

$$\begin{aligned} \Delta\mathbf{R}_{ij} &= \prod_{k=i}^{j-1} \mathbf{R}_B^O \mathrm{Exp}\left(\left(\widetilde{\boldsymbol{\omega}}_k - \mathbf{b}_{g_k} - \boldsymbol{\eta}_{gd}\right)\Delta t\right) \mathbf{R}_B^{O\,\mathrm{T}} \\ \Delta\mathbf{p}_{ij} &= \sum_{k=i+1}^{j} \Delta\mathbf{R}_{ik-1}\left(\widetilde{\boldsymbol{\psi}}_{O_k}^{O_{k-1}} - \boldsymbol{\eta}_{\psi d}\right) \end{aligned} \tag{14}$$

where $\mathbf{b}_{g_k} = \mathbf{b}_{g_i} + \sum_{n=i}^{k-1} \boldsymbol{\eta}_{b_g}\Delta t$, which is obtained by integrating (6). Since the gyroscope bias of keyframe i is known, the mean of $\mathbf{b}_{g_k}$ is $\mathbf{b}_{g_i}$ and $\delta\mathbf{b}_{g_{ik}} = \sum_{n=i}^{k-1} \boldsymbol{\eta}_{b_g}\Delta t$ is the bias noise. Bias noise $\delta\mathbf{b}_{g_{ik}}$ is a zero-mean Gaussian noise, since it is a linear combination of zero-mean Gaussian noise $\boldsymbol{\eta}_{b_g}$. Then by using the first-order approximation and dropping higher-order noise terms, we split each increment in (14) to preintegrated measurement and its noise. For rotation, we have:

$$\begin{aligned} \Delta\mathbf{R}_{ij} &= \prod_{k=i}^{j-1} \mathrm{Exp}\left(\mathbf{R}_B^O\left(\widetilde{\boldsymbol{\omega}}_k - \mathbf{b}_{g_i} - \delta\mathbf{b}_{g_{ik}} - \boldsymbol{\eta}_{gd}\right)\Delta t\right) \\ &\approx \prod_{k=i}^{j-1} \Big[\mathrm{Exp}\left(\mathbf{R}_B^O\left(\widetilde{\boldsymbol{\omega}}_k - \mathbf{b}_{g_i}\right)\Delta t\right) \\ &\qquad \times \mathrm{Exp}\left(-\mathbf{J}_{r_k}\mathbf{R}_B^O\left(\delta\mathbf{b}_{g_{ik}} + \boldsymbol{\eta}_{gd}\right)\Delta t\right)\Big] \\ &= \Delta\widetilde{\mathbf{R}}_{ij} \prod_{k=i}^{j-1} \mathrm{Exp}\left(-\Delta\widetilde{\mathbf{R}}_{k+1j}^{\mathrm{T}}\mathbf{J}_{r_k}\mathbf{R}_B^O(\delta\mathbf{b}_{g_{ik}} + \boldsymbol{\eta}_{gd})\Delta t\right) \\ &= \Delta\widetilde{\mathbf{R}}_{ij}\,\mathrm{Exp}\left(\delta\boldsymbol{\phi}_{ij}\right) \end{aligned} \tag{15}$$

where $\mathbf{J}_{r_k} = \mathbf{J}_r(\mathbf{R}_B^O(\widetilde{\boldsymbol{\omega}}_k - \mathbf{b}_{g_i})\Delta t)$ is the right Jacobian of SO(3). Therefore, we obtain the preintegrated rotation measurement:

$$\Delta\widetilde{\mathbf{R}}_{ij} = \prod_{k=i}^{j-1} \operatorname{Exp}\left(\mathbf{R}_B^O(\widetilde{\boldsymbol{\omega}}_k - \mathbf{b}_{g_i})\Delta t\right) \tag{16}$$

For position, we have:

$$\begin{aligned}\Delta\mathbf{p}_{ij} &\approx \sum_{k=i+1}^{j} \left[\Delta\widetilde{\mathbf{R}}_{ik-1}\left(\mathbf{I}_{3\times3} + \delta\boldsymbol{\phi}_{ik-1}^{\wedge}\right)\left(\widetilde{\boldsymbol{\psi}}_{O_k}^{O_{k-1}} - \boldsymbol{\eta}_{\psi d}\right)\right] \\ &= \sum_{k=i+1}^{j} \left[\Delta\widetilde{\mathbf{R}}_{ik-1}\left(\mathbf{I}_{3\times3}+\delta\boldsymbol{\phi}_{ik-1}^{\wedge}\right)\widetilde{\boldsymbol{\psi}}_{O_k}^{O_{k-1}} - \Delta\widetilde{\mathbf{R}}_{ik-1}\boldsymbol{\eta}_{\psi d}\right] \\ &= \Delta\widetilde{\mathbf{p}}_{ij} + \sum_{k=i+1}^{j}\left[-\Delta\widetilde{\mathbf{R}}_{ik-1}\widetilde{\boldsymbol{\psi}}_{O_k}^{O_{k-1}\wedge}\delta\boldsymbol{\phi}_{ik-1} - \Delta\widetilde{\mathbf{R}}_{ik-1}\boldsymbol{\eta}_{\psi d}\right] \\ &= \Delta\widetilde{\mathbf{p}}_{ij} + \delta\mathbf{p}_{ij}\end{aligned} \tag{17}$$

Therefore, we obtain the preintegrated position measurement:

$$\Delta\widetilde{\mathbf{p}}_{ij} = \sum_{k=i+1}^{j} \Delta\widetilde{\mathbf{R}}_{ik-1}\widetilde{\boldsymbol{\psi}}_{O_k}^{O_{k-1}} \tag{18}$$

C. NOISE PROPAGATION

As defined in Section IV-B, the bias noise is:

$$\delta\mathbf{b}_{g_{ij}} = \sum_{k=i}^{j-1} \boldsymbol{\eta}_{b_g}\Delta t \tag{19}$$

Then obtained from (15), the rotation noise is:

$$\delta\boldsymbol{\phi}_{ij} = \sum_{k=i}^{j-1}\left[-\Delta\widetilde{\mathbf{R}}_{k+1j}^{\mathrm{T}}\mathbf{J}_{r_k}\mathbf{R}_B^O\left(\delta\mathbf{b}_{g_{ik}} + \boldsymbol{\eta}_{gd}\right)\Delta t\right] \tag{20}$$

The rotation noise term $\delta\boldsymbol{\phi}_{ij}$ is zero-mean and Gaussian, since it is a linear combination of zero-mean white Gaussian noise $\boldsymbol{\eta}_{gd}$ and $\delta\mathbf{b}_{g_{ik}}$.

Furthermore, from (17), we obtain the position noise:

$$\delta\mathbf{p}_{ij} = \sum_{k=i+1}^{j}\left[-\Delta\widetilde{\mathbf{R}}_{ik-1}\widetilde{\boldsymbol{\psi}}_{O_k}^{O_{k-1}\wedge}\delta\boldsymbol{\phi}_{ik-1} - \Delta\widetilde{\mathbf{R}}_{ik-1}\boldsymbol{\eta}_{\psi d}\right] \tag{21}$$

The position noise $\delta\mathbf{p}_{ij}$ is also zero-mean Gaussian noise, because it is a linear combination of noise $\boldsymbol{\eta}_{\psi d}$ and rotation noise $\delta\boldsymbol{\phi}_{ik-1}$.

We write (19), (20) and (21) in iterative form, then the noise propagation can be written in matrix form as:

$$\begin{aligned}&\begin{bmatrix}\delta\boldsymbol{\phi}_{ik+1} \\ \delta\mathbf{p}_{ik+1} \\ \delta\mathbf{b}_{g_{ik+1}}\end{bmatrix} \\ &= \begin{bmatrix}\Delta\widetilde{\mathbf{R}}_{kk+1}^{\mathrm{T}} & \mathbf{0}_{3\times3} & -\mathbf{J}_{r_k}\mathbf{R}_B^O\Delta t \\ -\Delta\widetilde{\mathbf{R}}_{ik}\widetilde{\boldsymbol{\psi}}_{O_{k+1}}^{O_k\wedge} & \mathbf{I}_{3\times3} & \mathbf{0}_{3\times3} \\ \mathbf{0}_{3\times3} & \mathbf{0}_{3\times3} & \mathbf{I}_{3\times3}\end{bmatrix} \\ &\quad \cdot \begin{bmatrix}\delta\boldsymbol{\phi}_{ik} \\ \delta\mathbf{p}_{ik} \\ \delta\mathbf{b}_{g_{ik}}\end{bmatrix} + \begin{bmatrix}-\mathbf{J}_{r_k}\mathbf{R}_B^O\Delta t & \mathbf{0}_{3\times3} & \mathbf{0}_{3\times3} \\ \mathbf{0}_{3\times3} & -\Delta\widetilde{\mathbf{R}}_{ik} & \mathbf{0}_{3\times3} \\ \mathbf{0}_{3\times3} & \mathbf{0}_{3\times3} & \mathbf{I}_{3\times3}\Delta t\end{bmatrix}\begin{bmatrix}\boldsymbol{\eta}_{gd} \\ \boldsymbol{\eta}_{\psi d} \\ \boldsymbol{\eta}_{b_g}\end{bmatrix}\end{aligned} \tag{22}$$

or more simply:

$$\mathbf{n}_{ik+1} = \mathbf{A}\mathbf{n}_{ik} + \mathbf{B}\boldsymbol{\eta} \tag{23}$$

Given the linear model (23) and the covariance $\boldsymbol{\Sigma}_\eta \in \mathbb{R}^{9\times9}$ of odometer measurement noise $\boldsymbol{\eta}$, it is possible to compute the covariance of preintegrated odometer measurement noise iteratively:

$$\boldsymbol{\Sigma}_{\mathcal{O}_{ik+1}} = \mathbf{A}\boldsymbol{\Sigma}_{\mathcal{O}_{ik}}\mathbf{A}^{\mathrm{T}} + \mathbf{B}\boldsymbol{\Sigma}_\eta\mathbf{B}^{\mathrm{T}} \tag{24}$$

with initial condition $\boldsymbol{\Sigma}_{\mathcal{O}_{ii}} = \mathbf{0}_{9\times9}$.

Therefore, we can fully characterize the preintegrated odometer measurement noise as:

$$\mathbf{n}_{ij} = \begin{bmatrix}\delta\boldsymbol{\phi}_{ij}^{\mathrm{T}} & \delta\mathbf{p}_{ij}^{\mathrm{T}} & \delta\mathbf{b}_{g_{ij}}^{\mathrm{T}}\end{bmatrix}^{\mathrm{T}} \sim \mathcal{N}\left(\mathbf{0}_{9\times1}, \boldsymbol{\Sigma}_{\mathcal{O}_{ij}}\right) \tag{25}$$

D. BIAS UPDATE

In the previous section, we assumed that the gyroscope bias $\mathbf{b}_{g_i}$ is fixed. Given the bias change $\mathbf{b}_{g_i} \leftarrow \bar{\mathbf{b}}_{g_i} + \delta\mathbf{b}_{g_i}$, we can update the preintegrated measurements by using the first-order approximation. For preintegrated rotation measurement:

$$\begin{aligned}&\Delta\widetilde{\mathbf{R}}_{ij}\left(\mathbf{b}_{g_i}\right) \\ &= \prod_{k=i}^{j-1}\operatorname{Exp}\left(\mathbf{R}_B^O\left(\widetilde{\boldsymbol{\omega}}_k - \bar{\mathbf{b}}_{g_i} - \delta\mathbf{b}_{g_i}\right)\Delta t\right) \\ &\approx \prod_{k=i}^{j-1}\left[\operatorname{Exp}\left(\mathbf{R}_B^O\left(\widetilde{\boldsymbol{\omega}}_k - \bar{\mathbf{b}}_{g_i}\right)\Delta t\right)\operatorname{Exp}\left(-\mathbf{J}_{r_k}\mathbf{R}_B^O\delta\mathbf{b}_{g_i}\Delta t\right)\right] \\ &= \Delta\widetilde{\mathbf{R}}_{ij}\left(\bar{\mathbf{b}}_{g_i}\right)\prod_{k=i}^{j-1}\operatorname{Exp}\left(-\Delta\widetilde{\mathbf{R}}_{k+1j}^{\mathrm{T}}\mathbf{J}_{r_k}\mathbf{R}_B^O\delta\mathbf{b}_{g_i}\Delta t\right) \\ &= \Delta\widetilde{\mathbf{R}}_{ij}\left(\bar{\mathbf{b}}_{g_i}\right)\operatorname{Exp}\left(\frac{\partial\Delta\bar{\mathbf{R}}_{ij}}{\partial\mathbf{b}_{g_i}}\delta\mathbf{b}_{g_i}\right)\end{aligned} \tag{26}$$

where $\frac{\partial\Delta\bar{\mathbf{R}}_{ij}}{\partial\mathbf{b}_{g_i}} = \sum_{k=i}^{j-1} -\Delta\widetilde{\mathbf{R}}_{k+1j}^{\mathrm{T}}\mathbf{J}_{r_k}\mathbf{R}_B^O\Delta t$. For preintegrated position measurement:

$$\begin{aligned}&\Delta\widetilde{\mathbf{p}}_{ij}\left(\mathbf{b}_{g_i}\right) \\ &= \sum_{k=i+1}^{j}\Delta\widetilde{\mathbf{R}}_{ik-1}\left(\bar{\mathbf{b}}_{g_i}\right)\operatorname{Exp}\left(\frac{\partial\Delta\bar{\mathbf{R}}_{ik-1}}{\partial\mathbf{b}_{g_i}}\delta\mathbf{b}_{g_i}\right)\widetilde{\boldsymbol{\psi}}_{O_k}^{O_{k-1}} \\ &\approx \sum_{k=i+1}^{j}\Delta\widetilde{\mathbf{R}}_{ik-1}\left(\bar{\mathbf{b}}_{g_i}\right)\left(\mathbf{I}_{3\times3} + \left(\frac{\partial\Delta\bar{\mathbf{R}}_{ik-1}}{\partial\mathbf{b}_{g_i}}\delta\mathbf{b}_{g_i}\right)^{\wedge}\right)\widetilde{\boldsymbol{\psi}}_{O_k}^{O_{k-1}} \\ &= \Delta\widetilde{\mathbf{p}}_{ij}\left(\bar{\mathbf{b}}_{g_i}\right) - \sum_{k=i+1}^{j}\Delta\widetilde{\mathbf{R}}_{ik-1}\left(\bar{\mathbf{b}}_{g_i}\right)\widetilde{\boldsymbol{\psi}}_{O_k}^{O_{k-1}\wedge}\frac{\partial\Delta\bar{\mathbf{R}}_{ik-1}}{\partial\mathbf{b}_{g_i}}\delta\mathbf{b}_{g_i} \\ &= \Delta\widetilde{\mathbf{p}}_{ij}\left(\bar{\mathbf{b}}_{g_i}\right) + \frac{\partial\Delta\bar{\mathbf{p}}_{ij}}{\partial\mathbf{b}_{g_i}}\delta\mathbf{b}_{g_i}\end{aligned} \tag{27}$$

where $\frac{\partial\Delta\bar{\mathbf{p}}_{ij}}{\partial\mathbf{b}_{g_i}} = \sum_{k=i+1}^{j} -\Delta\widetilde{\mathbf{R}}_{ik-1}(\bar{\mathbf{b}}_{g_i})\widetilde{\boldsymbol{\psi}}_{O_k}^{O_{k-1}\wedge}\frac{\partial\Delta\bar{\mathbf{R}}_{ik-1}}{\partial\mathbf{b}_{g_i}}$.

E. PREINTEGRATED ODOMETER FACTOR

From the geometric relation between two consecutive keyframes i and j, we get our preintegrated odometer measurement model as:

$$\begin{aligned}\mathbf{R}_W^{O_i}\mathbf{R}_W^{O_j\mathrm{T}} &= \Delta\widetilde{\mathbf{R}}_{ij}\left(\mathbf{b}_{g_i}\right)\mathrm{Exp}\left(\delta\boldsymbol{\phi}_{ij}\right)\\ -\mathbf{R}_W^{O_i}\mathbf{R}_W^{O_j\mathrm{T}}\mathbf{p}_W^{O_j}+\mathbf{p}_W^{O_i} &= \Delta\widetilde{\mathbf{p}}_{ij}(\mathbf{b}_{g_i})+\delta\mathbf{p}_{ij}\end{aligned} \tag{28}$$

Therefore, the preintegrated odometer residual $\mathbf{r}_{\mathcal{O}_{ij}} = \left[\mathbf{r}^{\mathrm{T}}_{\Delta\mathbf{R}_{ij}}, \mathbf{r}^{\mathrm{T}}_{\Delta\mathbf{p}_{ij}}, \mathbf{r}^{\mathrm{T}}_{\Delta\mathbf{b}_{g_{ij}}}\right]^{\mathrm{T}} \in \mathbb{R}^9$ can be defined as:

$$\begin{aligned}\mathbf{r}_{\Delta\mathbf{R}_{ij}} &= \mathrm{Log}\left(\left(\Delta\widetilde{\mathbf{R}}_{ij}\left(\bar{\mathbf{b}}_{g_i}\right)\mathrm{Exp}\left(\frac{\partial\Delta\bar{\mathbf{R}}_{ij}}{\partial\mathbf{b}_{g_i}}\delta\mathbf{b}_{g_i}\right)\right)^{\mathrm{T}}\mathbf{R}_W^{O_i}\mathbf{R}_W^{O_j\mathrm{T}}\right)\\ \mathbf{r}_{\Delta\mathbf{p}_{ij}} &= -\mathbf{R}_W^{O_i}\mathbf{R}_W^{O_j\mathrm{T}}\mathbf{p}_W^{O_j}+\mathbf{p}_W^{O_i}-\left(\Delta\widetilde{\mathbf{p}}_{ij}(\bar{\mathbf{b}}_{g_i})+\frac{\partial\Delta\bar{\mathbf{p}}_{ij}}{\partial\mathbf{b}_{g_i}}\delta\mathbf{b}_{g_i}\right)\\ \mathbf{r}_{\Delta\mathbf{b}_{g_{ij}}} &= \mathbf{b}_{g_j}-\mathbf{b}_{g_i}\end{aligned} \tag{29}$$

F. VISUAL FACTOR

According to the measurement model in (4), the l^{th} map point expressed in the world reference frame $\{W\}$ is projected onto the image plane of the i^{th} keyframe as:

$$\mathbf{z}_{il} = \pi(\mathbf{R}_O^C\mathbf{R}_W^{O_i}\mathbf{f}_l^W+\mathbf{R}_O^C\mathbf{p}_W^{O_i}+\mathbf{p}_O^C) \tag{30}$$

Therefore, the reprojection error $\mathbf{r}_{\mathcal{C}_{il}} \in \mathbb{R}^2$ for the l^{th} map point seen by the i^{th} keyframe is:

$$\mathbf{r}_{\mathcal{C}_{il}} = \mathbf{z}_{il}-\widetilde{\mathbf{z}}_{il} \tag{31}$$

G. PLANE FACTOR

The x-y plane of the first wheel frame $\{O_1\}$ coincides with the physical plane. Thus, we express the plane factor $\mathbf{r}_{\mathrm{pl}_k} \in \mathbb{R}^3$ as:

$$\mathbf{r}_{\mathrm{pl}_k} = \begin{bmatrix}\left[\,\mathbf{e}_1\ \mathbf{e}_2\,\right]^{\mathrm{T}}\mathbf{R}_W^{O_k}\mathbf{R}_W^{O_1\mathrm{T}}\mathbf{e}_3\\ \mathbf{e}_3^{\mathrm{T}}\left(-\mathbf{R}_W^{O_1}\mathbf{R}_W^{O_k\mathrm{T}}\mathbf{p}_W^{O_k}+\mathbf{p}_W^{O_1}\right)\end{bmatrix}-\widetilde{\mathbf{pl}}_k \tag{32}$$

where $\mathbf{e}_1 = \left[\,1\ 0\ 0\,\right]^{\mathrm{T}}$, $\mathbf{e}_2 = \left[\,0\ 1\ 0\,\right]^{\mathrm{T}}$ and $\mathbf{e}_3 = \left[\,0\ 0\ 1\,\right]^{\mathrm{T}}$.

The first two elements in (32) is the planar rotational constraint, it means that rotating $\mathbf{e}_3$ vector in frame $\{O_1\}$ to frame $\{O_k\}$, the result should also be $\mathbf{e}_3$. The result is equal to $\mathbf{e}_3$ if and only if the roll and pitch angles between frames $\{O_1\}$ and $\{O_k\}$ are all zero. Thus, constraining the first two elements in the residual to zero corresponds to constraining the roll and pitch angles between two frames to zero. The third element in (32) is the planar translational constraint, which means that z-axis translation between frames $\{O_1\}$ and $\{O_k\}$ should be zero. In addition, the covariance of planar measurement $\boldsymbol{\Sigma}_{\mathrm{pl}}$ is set as diag(0.0012, 0.0012, 0.0004) in this paper to allow 2° deviation for roll and pitch angles and 0.02m deviation for z-axis translation.

V. MONOCULAR VOSLAM SYSTEM

Our monocular VOSLAM system is inspired by ORB-SLAM [14] and ORB-VISLAM [5]. Fig. 1 shows an overview of the proposed system. In this section, we detail the main changes of our VOSLAM system with respect to the referenced system.

A. MAP INITIALIZATION

The map initialization is in charge of estimating two initial values. Firstly, we estimate the initial value of gyrosocpe bias $\mathbf{b}_g$. This calculation is not necessary, however computing its initial value can achieve better accuracy as shown in the seventh and eighth columns of Table 2, so we compute the initial $\mathbf{b}_g$ in this paper. Then we construct the initial map with scale.

The steps of map initialization are as follows. Firstly, we search for feature matches between current frame k and reference frame r. If there are sufficient feature matches, we add this frame to the local window of gyroscope bias initialization and perform the next step, else we set the current frame as reference frame and clear the local window. The second step is to check the parallax of each correspondence and pick out a set of feature matches $\mathcal{F}$ that have sufficient parallax. When the size of $\mathcal{F}$ is greater than a threshold, we perform the next step. The next steps are different depending on whether to estimate the initial value of $\mathbf{b}_g$.

If we estimate the initial value of gyroscope bias, in the third step, we firstly compute the up-to-scale relative transformation $\mathbf{T}_{C_k}^{C_r}$ between reference frame r and current frame k by using the Five-point algorithm [28], and triangulate the feature matches $\mathcal{F}$. Then if the size of successfully triangulated map points is larger than a threshold, we compute the poses $\mathbf{T}_{C_i}^{C_r}$ of all frames in the local window by using the perspective-n-point (PnP) method [29], and perform a pure visual global BA to optimize the pose of all frames in the local window. If the size of successfully triangulated map points is still larger than a threshold after the optimization, we perform the next step. In step four, we compute the preintegrated odometer measurements $\Delta\widetilde{\mathbf{R}}_{ri}$ for all the frames in the local window of gyroscope bias initialization, and combine it with the computed relative rotations $\mathbf{R}_{O_i}^{O_r} = \mathbf{R}_O^{C\,\mathrm{T}}\mathbf{R}_{C_i}^{C_r}\mathbf{R}_O^C$ from the last step to estimate the initial gyroscope bias:

$$\underset{\mathbf{b}_g}{\mathrm{argmin}}\sum_{i=r+1}^{k}\left\|\mathrm{Log}\left(\left(\Delta\widetilde{\mathbf{R}}_{ri}\mathrm{Exp}\left(\frac{\partial\Delta\bar{\mathbf{R}}_{ri}}{\partial\mathbf{b}_g}\mathbf{b}_g\right)\right)^{\mathrm{T}}\mathbf{R}_{O_i}^{O_r}\right)\right\|^2 \tag{33}$$

which is derived from (26) (28). Next, based on the estimated gyroscope bias $\mathbf{b}_g$, we re-compute the odometer preintegration terms $\Delta\widetilde{\mathbf{R}}_{rk}$ and $\Delta\widetilde{\mathbf{p}}_{rk}$, and reset the pose of current frame as $\mathbf{T}_W^{O_k} = \Delta\widetilde{\mathbf{T}}_{rk}^{-1}\mathbf{T}_W^{O_r}$. The pose of reference frame $\mathbf{T}_W^{O_r}$ can be set to arbitrary value, we set it to the identity in this paper. Then we use the re-computed poses to re-triangulate the matched features $\mathcal{F}$.

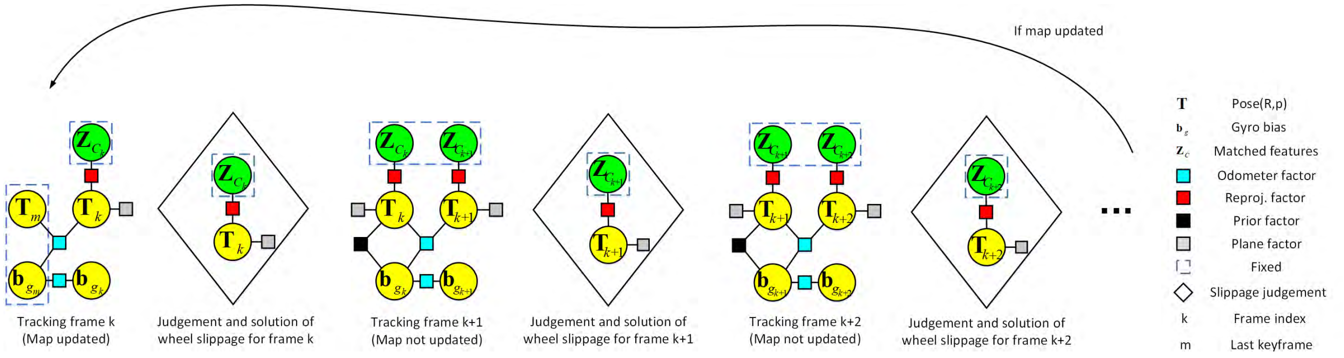

FIGURE 3. Evolution of the factor graph in motion tracking when the last visual tracking is successful. If map is updated, we optimize the state of frame k by connecting an odometer factor to last keyframe m. If map is not changed, state of both last frame $k-1$ and current frame k are jointly optimized by linking an odometer factor between them and adding a prior factor to last frame $k-1$. The prior for last frame $k-1$ is obtained from the last optimization. At the end of each joint optimization, based on the optimized result, we determine whether the wheel slippage has occurred. If wheel slippage is detected, the pose of frame k is re-optimized by using the factor graph in diamond.

If we do not estimate the initial value of $\mathbf{b}_g$, in the third step, we compute the preintegrated transformation measurement $\Delta\widetilde{\mathbf{T}}_{rk}$ between reference frame r and current frame k, and set the pose of current frame as $\mathbf{T}_W^{O_k} = \Delta\widetilde{\mathbf{T}}_{rk}^{-1}\mathbf{T}_W^{O_r}$. Then we triangulate the matched features $\mathcal{F}$.

When the size of successfully created map points is greater than a threshold, we set the reference frame and current frame as keyframes. These two initial keyframs and the constructed initial map points constitute the initial map. Finally, a global BA that minimizes all the reprojection factors, odometer factors, and plane factors contained in the initial map is performed to refine the initial map.

B. TRACKING WHEN LAST VISUAL TRACKING IS SUCCESSFUL

For tracking the motion of current frame when the last visual tracking is successful, we firstly use the odometer measurements to predict the initial pose of current frame. Based on the initial pose, we match the keypoints extracted from the current frame to the map points seen by last frame. Then we use all the available visual and odometer measurements to optimize the state of current frame. The confidence of last state estimate is different according to whether the map is updated in back-end, thus we adopt different strategies to track the motion of current frame depending on whether the map is updated. When the map is updated in back-end, the state of last keyframe optimized by local BA or pose graph optimization has high confidence, so we fix the optimized state of last keyframe to optimize the state of current frame as described in Section V-B1. Then when the map is not updated in back-end, the last state optimized by motion tracking is not as confident as the state optimized in back-end, so instead of fixing last state estimate, we add a prior to the state of last frame to optimize the state of current frame as described in Section V-B2. Finally, according to the optimized result, we use strategy described in Section V-B3 to detect and solve the wheel slippage. The tracking mechanism is illustrated graphically in Fig. 3.

1) TRACKING WHEN MAP IS UPDATED

When the motion tracking is performed just after the map is updated in back-end, we firstly compute the preintegrated odometer measurement between current frame k and last keyframe m. Then the preintegration terms $\Delta\mathbf{R}_{O_k}^{O_m}$ and $\Delta\mathbf{p}_{O_k}^{O_m}$ are combined with the optimized pose of last keyframe to predict the initial pose of current frame. Finally, we optimize the state of current frame k by minimizing the following energy function:

$$\boldsymbol{\gamma} = \{\boldsymbol{x}_k\}$$

$$\boldsymbol{\gamma}^* = \operatorname*{argmin}_{\boldsymbol{\gamma}}\left(\sum_{l\in\mathcal{M}_{C_k}} \|\mathbf{r}_{\mathcal{C}_{kl}}\|^2_{\boldsymbol{\Sigma}_{\mathcal{C}_{kl}}} + \|\mathbf{r}_{\mathcal{O}_{mk}}\|^2_{\boldsymbol{\Sigma}_{\mathcal{O}_{mk}}} + \|\mathbf{r}_{\mathrm{pl}_k}\|^2_{\boldsymbol{\Sigma}_{\mathrm{pl}}}\right) \tag{34}$$

where $\mathcal{M}_{C_k}$ denotes the feature matches of current frame. After the optimization, the resulting estimation and Hessian matrix are served as a prior for the next optimization.

2) TRACKING WHEN MAP IS NOT UPDATED

When the map is not updated in back-end, we compute the odometer preintegration terms $\Delta\mathbf{R}_{O_k}^{O_{k-1}}$ and $\Delta\mathbf{p}_{O_k}^{O_{k-1}}$ between current frame k and last frame $k-1$, and combine it with the pose of last frame to predict the initial pose of current frame. Then we optimize the state of current frame k by performing the nonlinear optimization that minimizing the following objective function:

$$\begin{aligned}\boldsymbol{\gamma} &= \{\boldsymbol{x}_{k-1}, \boldsymbol{x}_k\}\\ \boldsymbol{\gamma}^* &= \operatorname*{argmin}_{\boldsymbol{\gamma}}\Big(\sum_{l\in\mathcal{M}_{C_{k-1}}} \|\mathbf{r}_{\mathcal{C}_{k-1l}}\|^2_{\boldsymbol{\Sigma}_{\mathcal{C}_{k-1l}}} + \sum_{n\in\mathcal{M}_{C_k}} \|\mathbf{r}_{\mathcal{C}_{kn}}\|^2_{\boldsymbol{\Sigma}_{\mathcal{C}_{kn}}}\\ &\quad + \|\mathbf{r}_{\mathcal{O}_{k-1k}}\|^2_{\boldsymbol{\Sigma}_{\mathcal{O}_{k-1k}}} + \|\mathbf{r}_{0_{k-1}}\|^2_{\boldsymbol{\Sigma}_{0_{k-1}}}\\ &\quad + \|\mathbf{r}_{\mathrm{pl}_{k-1}}\|^2_{\boldsymbol{\Sigma}_{\mathrm{pl}}} + \|\mathbf{r}_{\mathrm{pl}_k}\|^2_{\boldsymbol{\Sigma}_{\mathrm{pl}}}\Big)\end{aligned} \tag{35}$$

where the residual $\mathbf{r}_{0_{k-1}} = \left[\mathbf{r}^{\mathrm{T}}_{\mathbf{R}_{k-1}} \; \mathbf{r}^{\mathrm{T}}_{\mathbf{p}_{k-1}} \; \mathbf{r}^{\mathrm{T}}_{\mathbf{b}_{g_{k-1}}} \right]^{\mathrm{T}} \in \mathbb{R}^9$ is a prior error term of last frame:

$$\begin{aligned}
\mathbf{r}_{\mathbf{R}_{k-1}} &= \mathrm{Log}\left(\widetilde{\mathbf{R}}_W^{O_{k-1}\mathrm{T}} \mathbf{R}_W^{O_{k-1}}\right) \\
\mathbf{r}_{\mathbf{p}_{k-1}} &= \mathbf{p}_W^{O_{k-1}} - \widetilde{\mathbf{p}}_W^{O_{k-1}} \\
\mathbf{r}_{\mathbf{b}_{g_{k-1}}} &= \mathbf{b}_{g_{k-1}} - \widetilde{\mathbf{b}}_{g_{k-1}}
\end{aligned} \tag{36}$$

where $\widetilde{\mathbf{R}}_W^{O_{k-1}}$, $\widetilde{\mathbf{p}}_W^{O_{k-1}}$, $\widetilde{\mathbf{b}}_{g_{k-1}}$, and $\mathbf{\Sigma}_{0_{k-1}}$ are the state and covariance matrix computed from the last pose optimization. The optimized result is also served as a prior for the next optimization.

3) DETECTING AND SOLVING WHEEL SLIPPAGE

Wheel encoder is an ambivalent sensor, it provides reliable traveled distance measurements of each wheel at most of time, but it can also deliver a very faulty data when wheel experiences a slippage. If we perform visual-odometric joint optimization using this kind of faulty data, in order to simultaneously satisfy the constraints of both odometer measurements with slippage and visual measurements, the optimization will result in a false estimate. Therefore, we provide a strategy to detect and solve this case. We think the current frame k experienced a slippage if the above visual-odometric optimization (34) (35) makes more than half of the originally matched features become outliers. Once the wheel slippage is detected, we set a slippage flag to current frame and reset the initial state of current frame k as the state of last frame $k-1$. Then we re-match the features of current frame to the map points seen by last frame. Finally, we only use those matched features to optimize the state of current frame:

$$\begin{aligned}
\boldsymbol{\gamma} &= \{\boldsymbol{x}_k\} \\
\boldsymbol{\gamma}^* &= \underset{\boldsymbol{\gamma}}{\mathrm{argmin}} \left(\sum_{l \in \mathcal{M}_{C_k}} \|\mathbf{r}_{\mathcal{C}_{kl}}\|^2_{\mathbf{\Sigma}_{\mathcal{C}_{kl}}} + \|\mathbf{r}_{\mathrm{pl}_k}\|^2_{\mathbf{\Sigma}_{\mathrm{pl}}} \right)
\end{aligned} \tag{37}$$

In this way, we can detect and solve the wheel slippage efficiently. Therefore, the system can provide the accurate state estimate all the time.

C. TRACKING WHEN LAST VISUAL TRACKING IS LOST

If visual information is not available for the motion tracking of current frame, we can only use the odometer measurements to compute the pose of current frame. Therefore, in order to obtain more accurate state estimate, we should make the visual information available as early as possible.

Supposing the last visual tracking is lost, then one of the three cases will happen for the current frame: (1) the robot revisits to an already reconstructed area; (2) the robot visits to a new environment where exists sufficient features; (3) the visual features are still unavailable wherever the robot is. For these different situations, we perform different strategies to estimate the pose of current frame. For case 1, a global relocalization method as done in [14], i.e. using DBOW [15] and PnP algorithm [29], is performed to compute the pose of current frame and render the visual information available. For case 2, based on the poses estimated from the solution of case 3, we re-perform the map initialization procedure described in Section V-A to construct a new map that is connected to the previous map, thereby making the visual information available. For case 3, we use the odometer measurements to compute the pose of current frame, which improves the robustness of our system to visual loss.

When enough features are extracted from the current frame, we firstly think the robot may returned to an already reconstructed environment and perform the global relocaliation method (solution for case 1). However, if the relocalization has continuously failed for 20 frames with enough features, we think the robot entered into a new environment and then construct a new map as solution for case 2. We deem the visual information becomes available for the motion tracking of current frame when the pose of current frame is supported by enough matched features. So if the pose is not supported by enough matched features or fewer features are extracted from the current frame, we think the visual information is still unavailable for the motion tracking of current frame and set the pose of current frame as solution for case 3.

D. TRACK LOCAL MAP AND KEYFRAME SELECTION

When the current visual tracking is successful, we match the features in current frame to the local map for constructing a compact covisibility graph, which can greatly improve the accuracy of system. Then we insert a keyframe to back-end when the following criteria are satisfied: (1) current frame tracks less than 90% features than last keyframe; (2) Local BA is finished in back-end. These criteria ensure a good visual tracking of the system.

E. BACK-END

The back-end includes the local mapping thread and the loop closing thread as paper [5], [14]. In local mapping thread, we update the covisibility graph, construct the new map points, and optimize the local map. When new keyframe k is inserted to the local mapping thread, we make a small change in local BA with respect to paper [5]. Visual-odometric local BA minimizing the cost function (13) is performed to optimize the last N keyframes in local window and all the map points seen by those N keyframes. One thing to note is that the odometer constraint linking to the last keyframe is only constructed for those keyframes without slippage flag. The loop closing thread is in charge of eliminating the accumulated drift when returning to an already reconstructed area, it is implemented in the same way as paper [5].

VI. EXPERIMENTS

In the following, we perform a number of experiments to evaluate the proposed VOSLAM system. Firstly in Section VI-A and Section VI-B, we perform the qualitative and quantitative analysis to show the accuracy of our system. Then the validity of the proposed strategy for detecting and solving wheel slippage is demonstrated in Section VI-C. Finally in

Section VI-D, we test the robustness of our algorithm to visual loss. The experiments are performed on a laptop with an Intel Core i5 2.2GHz CPU and 8GB RAM. The corresponding videos are available at: https://youtu.be/EaDTC92hQpc.

A. ALGORITHM EVALUATION ON DS DATASET

The DS dataset is provided by the author of [2], it is the dataset 1 in [2]. The dataset is recorded by a Pioneer 3 DX robot with a Project Tango, it provides 640 × 480 grayscale images at 30 Hz, the inertial measurements at 100Hz, and wheel encoder measurements at 10 Hz. In addition, the dataset also provides the ground truth that is computed from the batch least squares offline by using all the available visual, inertial, and wheel measurements.

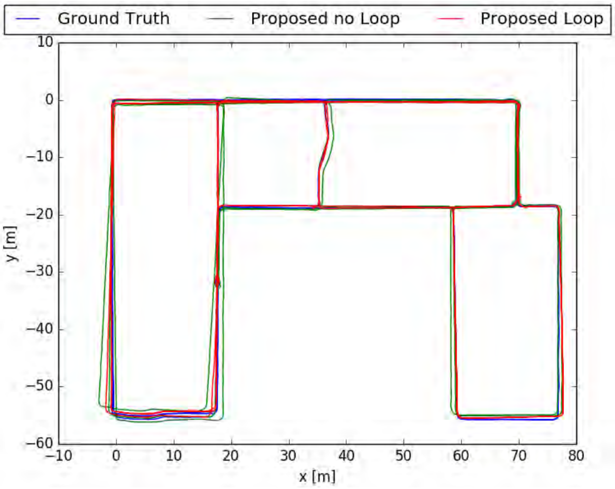

FIGURE 4. Comparison between the estimated trajectories and the ground truth.

Qualitative comparison of the estimated trajectories by our method without and with loop closure is shown in Fig. 4. The estimated trajectories and the ground truth are aligned in closed form by using the method of Horn [30]. We can qualitatively compare the estimated trajectories with the result provided in figure 6 of paper [2]. Firstly, by comparing the estimated trajectory from our algorithm without loop closure to the result estimated from state-of-the-art visual-inertial-odometric SLAM system [2], we can know that our algorithm without loop closure produces more accurate trajectory estimate than method [2]. The improvement is achieved by 1) tightly fusing the visual and odometer measurements in the optimization framework; 2) performing complete visual-odometric tracking strategies; 3) performing local BA that contains many covisibility information and inter-frame odometric constraints. Then by further comparison, it is clear that our algorithm with loop closure achieves better accuracy than our algorithm without loop closure, and thereby certainly achieves better accuracy than method [2], which is achieved by eliminating the accumulated error when returning to an already mapped area. Quantitatively, the sequence is 1080m long, and the positioning Root Mean Square Error (RMSE) of our algorithm without and with loop closure is 1.001m and 0.606m respectively, it is 0.093% and 0.056% of the total traveled distance with a comparison to 0.25% of the approach [2].

We also performed this sequence on the state-of-the-art and open-source monocular VSLAM system ORB-SLAM [14] and monocular VISLAM system VINS-MONO [6], [26] for comparison. ORB-SLAM is the base of our system, which successfully ran the sequence and reached the translation RMSE of 2.787m, the translation RMSE is computed by scaling the estimated trajectory to match the scale of ground truth. From the result, we can conclude that compared with the original monocular ORB-SLAM system, the proposed monocular VOSLAM system can not only recover the scale of the environment, but also achieve better accuracy. These improvements are achieved by 1) good scale initialization thanks to the reliable inter-frame odometer measurements; 2) tightly fusing the odometer factor with the visual factor of ORB-SLAM; 3) complete visual-odometric tracking mechanism that maximally exploits both measurements. However, VINS-MONO method fails to run through the sequence. After the visual-inertial alignment succeeds, the trajectory starts to drift in a short period of time, which is due to the special motion of the dataset. In most cases, the motion of the dataset is along the straight lines with constant velocity, VISLAM has additional unobservable directions (i.e. the scale of environment and the direction of local gravity) in the special motion, which makes the VINS-MONO unable to provide a good initial value for the dataset. Whereas, initialization is the most fragile step for tightly-coupled monocular VISLAM, thus in the dataset, the bad initialization causes the drift of the estimated trajectory.

B. ALGORITHM EVALUATION ON RAWSEEDS DATASET

We also evaluate our algorithm on four indoor sequences of the Rawseeds dataset. The dataset provides 320 × 240 images that are recorded by a forward-looking camera at frequency of 30Hz, and provides inertial measurements and wheel encoder measurements at 125Hz and 50Hz respectively. Besides, the ground truth is also provided for all the sequences. Since there are frame losses at the latter part of each sequence, we only use the reliable first 15000 frames of each sequence for algorithm comparison.

Firstly, we compare the proposed system with ORB-SLAM and VINS-MONO. In this section, in order to perform a fair comparison between the use of visual-odometric factor graph and the use of visual-inertial factor graph, we switch off the loop closure. A comparison of the translation RMSE for the estimated trajectories from different methods is shown in Table 1. X means that the corresponding method fails to run through the sequence. From the result, we can find that ORB-SLAM fails to run through the four sequences, which is because the sequences are relatively low-textured. In these sequences, most of the extracted and matched features are on the lines as shown in Fig. 5, thus faulty data

TABLE 1. Translation RMSE of the estimated trajectories from ORB-SLAM, VINS-MONO, and our method on the rawseeds dataset.

Sequence	ORB-SLAM(m)	VINS-MONO(m)	our method(m)
2009-02-25a	X	6.825	0.661
2009-02-25b	X	3.074	1.418
2009-02-26a	X	4.137	1.558
2009-02-27a	X	9.032	2.057

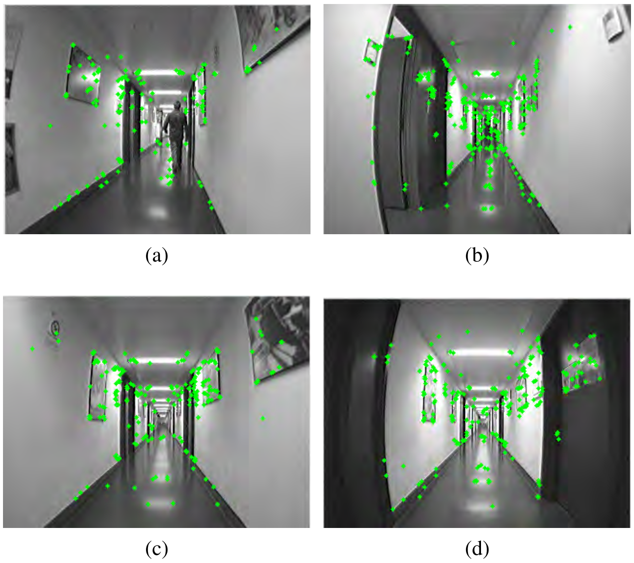
(a)
(b)
(c)
(d)

FIGURE 5. Tracked features in sample images of the rawseeds dataset.

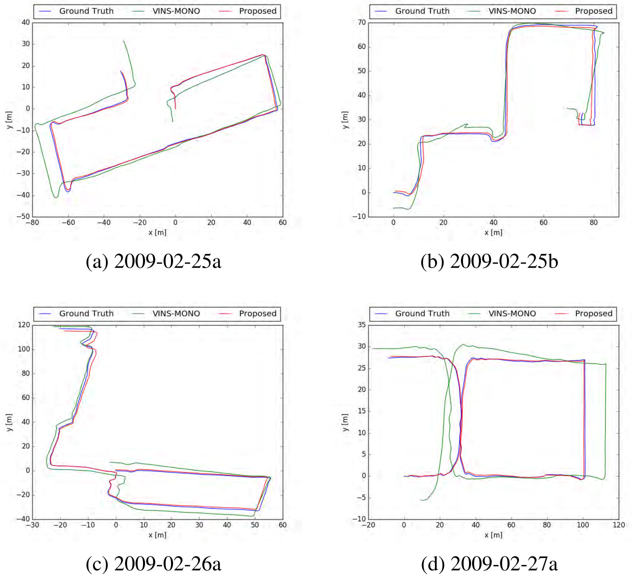

(a) 2009-02-25a
(b) 2009-02-25b
(c) 2009-02-26a
(d) 2009-02-27a

FIGURE 6. Comparison of the estimated trajectories from VINS-MONO and our algorithm with the ground truth on rawseeds dataset.

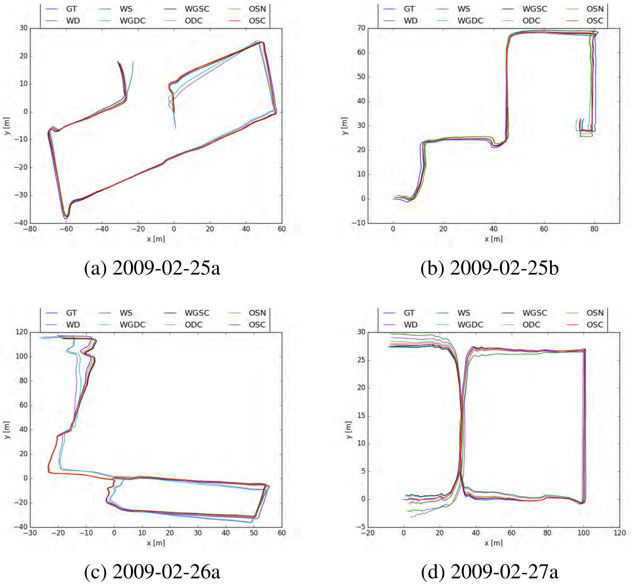

(a) 2009-02-25a
(b) 2009-02-25b
(c) 2009-02-26a
(d) 2009-02-27a

FIGURE 7. Comparison of the estimated trajectories from our system with different factor graphs on rawseeds dataset.

association causes the failure of motion tracking. However, VINS-MONO can run through the four sequences. The sequences do not go as straight as the ds dataset, so VINS-MONO can provide a good initial value that enables the system to successfully track the motion of subsequent frames. Qualitative comparison between VINS-MONO and our method is shown in Fig. 6. From the above quantitative and qualitative comparison, we can know that compared to VINS-MONO that uses visual and inertial measurements, our method using visual and odometer measurements can achieve better accuracy. It is due to the observability of these two systems under the special motion interested in this paper, which is discussed above. Therefore, we can conclude that our system that tightly fuses the visual and odometer measurements is more suitable for estimating the motion of ground robots.

Furthermore, we also compare the performance of our visual-odometric factor graph with the factor graphs that arbitrarily combine the visual measurements with wheel encoder, gyroscope, and planar measurements. In this comparison experiment, we also switch off the loop closure to fairly compare each factor graph. In the following, we abbreviate the proposed SE(3) preintegrated odometer factor as O, SE(2) wheel factor as W, SO(3) gyroscope factor as G, deterministic planar constraint as D, stochastic planar constraint as S, bg with computed initial value as C, bg with initial value of zero as N. Our factor graph contains OSC, and the factor graphs used for comparing with our factor graph are respectively containing 1) WD, 2)WS, 3) WGDC, 4) WGSC, 5) ODC, 6)OSN. Qualitative and Quantitative comparison between the six factor graphs and our factor graph are shown in Fig. 7 and Table 2.

From the result, we can know that our algorithm using the OSC factor graph achieves best accuracy. Compared to the use of factor graphs that respectively combine W, WGC, and OC with deterministic planar constraint D, the use of factor graphs that respectively combine W, WGC, and OC with stochastic planar constraint S improves the translation RMSE of 26%, 32%, and 14% respectively. The approximately in-plane motion of ground robots caused by uneven

TABLE 2. Translation RMSE of the estimated trajectories from our system with different factor graphs on rawseeds dataset.

Sequence	WD(m)	WS(m)	WGDC(m)	WGSC(m)	ODC(m)	OSN(m)	OSC(m)
2009-02-25a	2.343	0.779	1.718	0.793	0.910	1.145	0.661
2009-02-25b	1.691	2.235	1.879	1.615	1.603	2.293	1.418
2009-02-26a	3.323	1.831	3.527	1.790	1.731	1.945	1.558
2009-02-27a	2.806	2.676	2.587	2.445	2.408	2.583	2.057

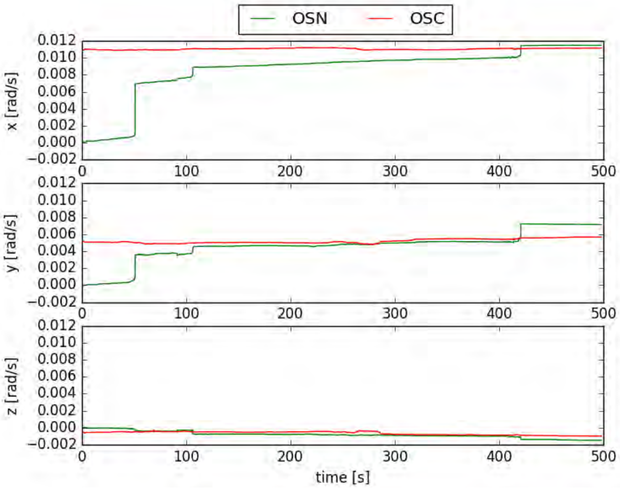

FIGURE 8. Comparison of the gyroscope bias estimate for 2009-02-25b sequence.

terrains and vibrations of the moving platform is better modeled by stochastic planar constraint, thus our system using the stochastic planar constraint achieves better accuracy than using the deterministic one. Then by comparing the second and third columns of the table to the sixth and eighth columns of the table, we can know that combining visual factor with the proposed SE(3) preintegrated odometer factor provides better accuracy than combining visual factor with the commonly used SE(2) wheel factor. Besides, when combining the visual measurements with wheel encoder measurements and gyroscope measurements, the factor graph using the proposed SE(3) preintegrated odometer factor provides better accuracy than the factor graph using the separate wheel encoder factor and gyroscope factor, which is demonstrated in the fifth and eighth columns of the table. The advantage of the proposed SE(3) preintegrated odometer factor is that compared to using the wheel encoder measurements and gyroscope measurements separately, tightly fusing these measurements can provide more accurate inter-frame rotational and translational constraint for both in-plane and out-of-plane motion. Finally by comparing the seventh and eighth columns of the table, we can know that computing an initial value for gyroscope bias can achieve better accuracy. Computing the initial gyroscope bias can accelerate the convergence of gyroscope bias to a stable value as shown in Fig. 8, which enables the system to get better rotational and translational constraint, thereby achieving better accuracy. The superiority of the proposed factor graph for localizing the ground robot will be more obvious when the motion of robot is often out of the plane constraint.

C. DEMONSTRATION OF ROBUSTNESS TO WHEEL SLIPPAGE

In the following experiments, we use data that is recorded from a DIY robot with a OV7251 camera mounted on it to look upward for visual sensing. The sensor suite provides the 640 × 480 grayscale images at frequency of 30Hz, the wheel odometer and gyroscope measurements at 50 Hz. Since there is no ground truth available, we just perform the qualitative analysis.

We firstly let the ground robot to walk normally, then hold the robot to make it static but the wheel is spinning, and finally let it to normally walk once again. The estimated results in some critical moments are shown in Fig. 9 and Fig. 10. Fig. 9a is the captured image at the first critical moment when the platform starts to experience wheel slippage, and the trajectories estimated by our method and the odometer from the beginning to this moment are shown in Fig. 10a. We can find that both methods accurately track the motion of robot under the normal motion. The image and the estimated trajectory obtained at the second moment when wheel slippage is over are given in Fig. 9b and Fig. 10b. As evident, the images captured at the first and second critical moments are almost the same. Although the odometer provides far away poses for these two moments due to wheel slippage, our method still gives the very close poses for these two moments. Therefore, the validity of the proposed strategy for detecting and solving wheel slippage can be proved. The reconstructed 3D map for the sequence are shown in Fig. 9c, the map is globally consistent, which is achieved by effectively solving the problem of wheel slippage.

Strategy for detecting and solving wheel slippage can also be used to solve the situation where the platform is moved artificially. For validation, we perform the experiment as follows. The sensor suite walks normally at first, then the platform is artificially moved to another location, during which time the wheels turn normally, and finally it normally walks once again. The test results for the situation are shown in Fig. 11 and Fig. 12. Before the sensor is moved away, the estimated trajectories from our method and the odometer are close to each other as shown in Fig. 12a. Fig. 11a and Fig. 11b are the captured images at the first moment when the platform starts to move and at the second moment when the platform has been moved to another location. As shown in Fig. 12b, for the artificial movement, our method provides

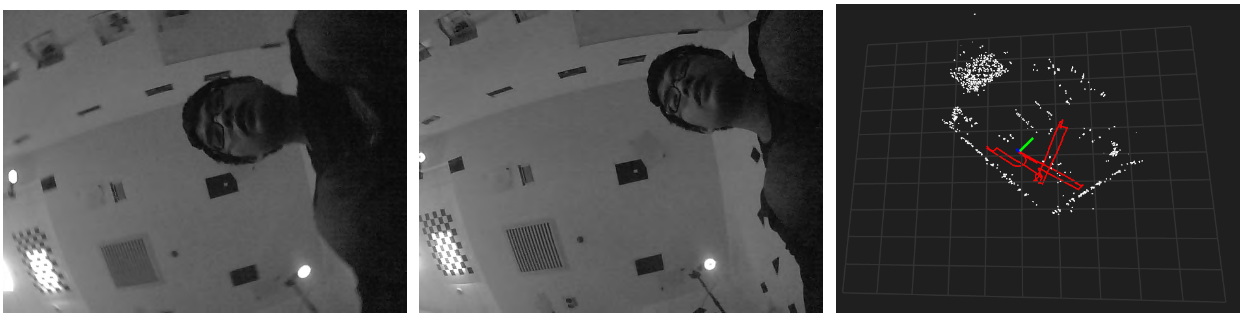

(a) wheel begins to slip (b) wheel slippage is over (c) end of sequence

FIGURE 9. **Captured images when the platform begins to experience wheel slippage and wheel slippage is over, and the finally reconstructed 3D map at the end of the sequence.**

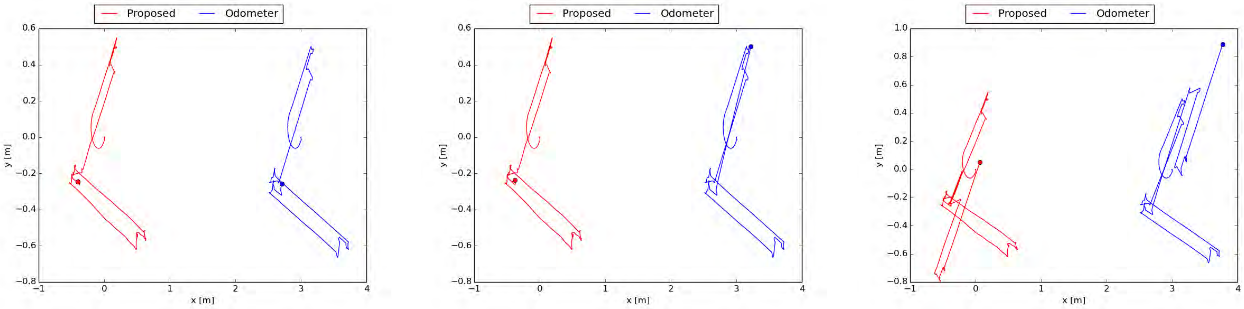

(a) wheel begins to slip (b) wheel slippage is over (c) end of sequence

FIGURE 10. **The estimated trajectories from the beginning to some critical moments.**

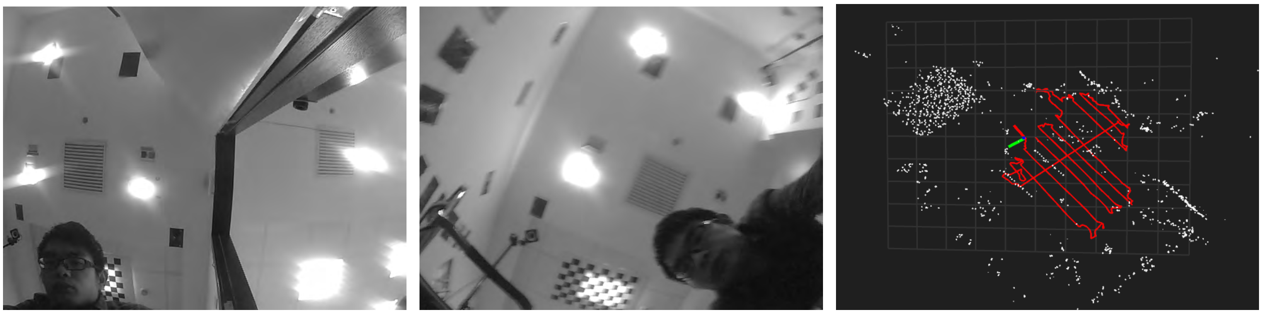

(a) platform begins to be moved (b) platform has been moved (c) end of sequence

FIGURE 11. **Captured images when the platform begins to be moved and the platform has been moved to another location, and the finally reconstructed 3D map at the end of the sequence.**

the precise motion tracking with a comparison to the faulty estimation of the odometer. Thereby, the effectiveness of the proposed strategy for detecting and solving faulty wheel measurements is demonstrated again.

D. DEMONSTRATION OF ROBUSTNESS TO VISUAL LOSS

The robustness of our system to visual loss is tested in two sequences, sequence 1 includes case 1 and case 3 described in Section V-C and the sequence 2 includes case 2 and case 3 described in Section V-C. Firstly, we use sequence 1 to test the proposed solution for case 1 and case 3, the estimated results in some critical moments are shown in Fig. 13 and Fig. 14. The robot firstly moves on areas where enough visual information is available to build a map of the environment shown in Fig. 13a. Then we turn off the lights to make the visual information unavailable. The motion of robot is continuously computed in the period of visual loss as shown in Fig. 14b, which is achieved by using the odometer measurements as the solution to case 3. Finally we turn on the lights, thus the robot revisits an already reconstructed area. As shown in the accompanying video, at that moment, the visual information is recovered, which is achieved by performing the global relocalization. The reconstructed map at the end of the sequence is shown in Fig. 13c, it is globally

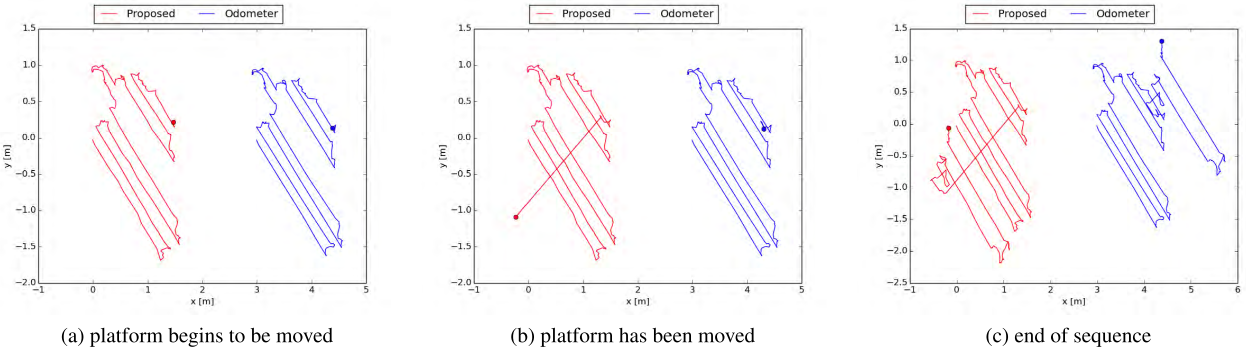

(a) platform begins to be moved

(b) platform has been moved

(c) end of sequence

FIGURE 12. The estimated trajectories from the beginning to some critical moments.

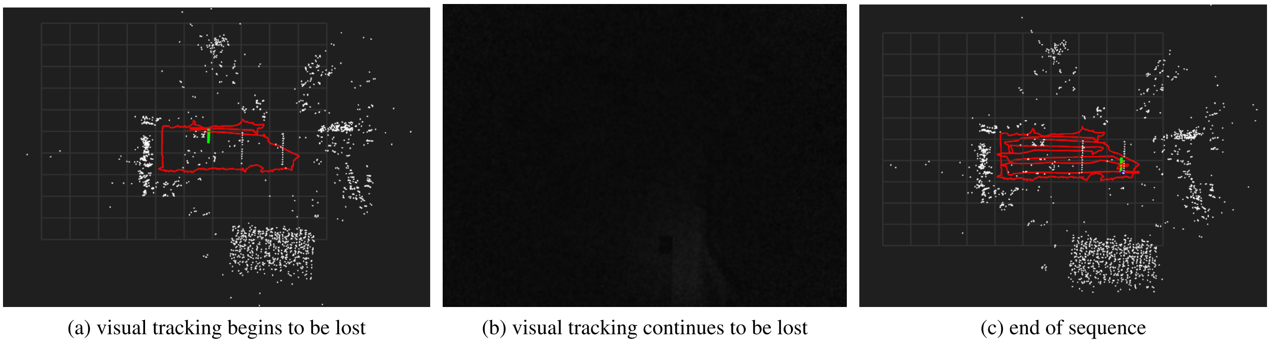

(a) visual tracking begins to be lost

(b) visual tracking continues to be lost

(c) end of sequence

FIGURE 13. Reconstructed 3D map when the visual tracking begins to be lost and at the end of the sequence, and captured image when visual tracking is lost.

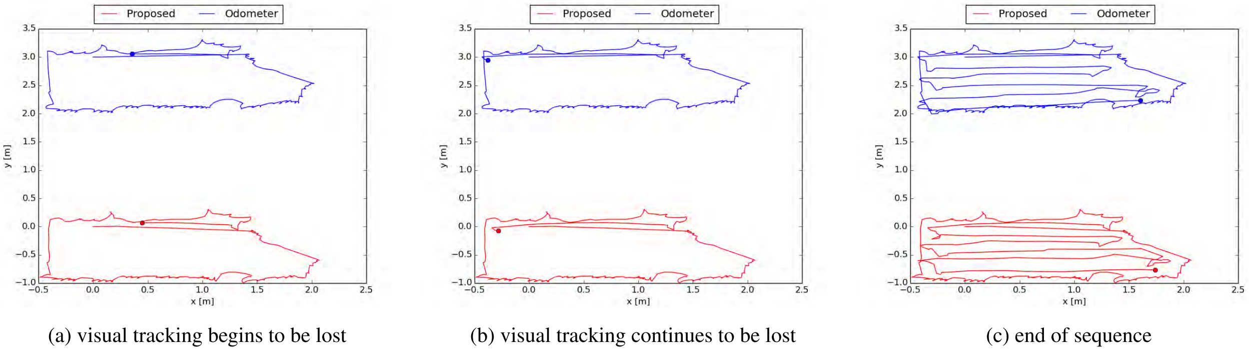

(a) visual tracking begins to be lost

(b) visual tracking continues to be lost

(c) end of sequence

FIGURE 14. The estimated trajectories from the beginning to some critical moments.

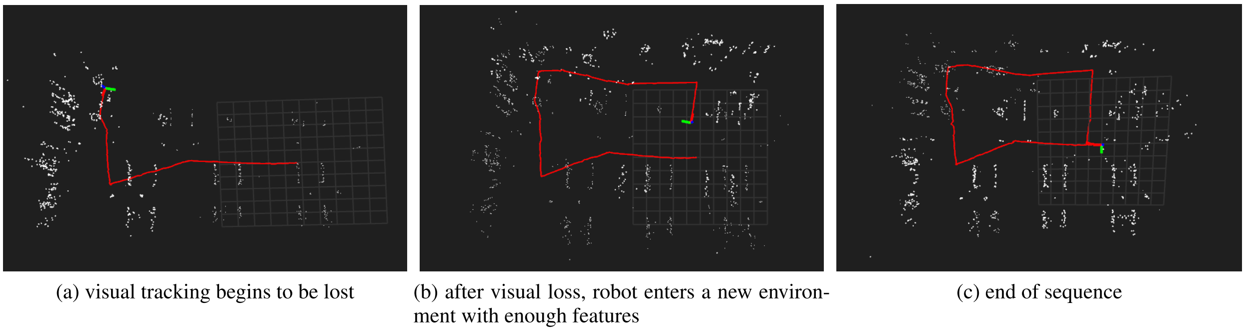

(a) visual tracking begins to be lost

(b) after visual loss, robot enters a new environment with enough features

(c) end of sequence

FIGURE 15. Reconstructed 3D map when the visual tracking begins to be lost, when the robot enters a new environment with enough features after the visual loss, and at the end of the sequence.

consistent without closing the loop. Therefore, we can validate the effectiveness of the proposed solution for case 1 and case 3.

Secondly, we use sequence 2 to test the proposed solution for case 2, the test results are shown in Fig. 15. The robot firstly moves on areas where enough visual information is available to build a map of the environment shown in Fig. 15a. Then the robot goes to a low-textured environment, and later enters a new environment where enough features are available. From Fig. 15b, we can know that the map of the new environment is created, however the new map is not consistent with the previously reconstructed map. Finally, the robot returns to a previously mapped area, which triggers the loop closure to eliminate the accumulated error, thereby constructing a globally consistent map shown in Fig. 15c. From the experiment, we can conclude that our system can not only tightly fuse both measurements to ensure the system accuracy, but also can improve the system robustness to visual loss by using the stable measurements from odometer.

VII. CONCLUSION AND FUTURE WORK

In this paper, we have proposed a tightly-coupled monocular VOSLAM system. The whole system is bootstrapped by the proposed map initialization method. Then when both visual and odometer measurements are available, our system tightly integrates the proposed preintegrated odometer factor with visual factor in the framework of optimization, which ensures the system accuracy. Besides, when the visual information is not available, our system tries to recover the visual information as soon as possible and improves the system robustness to visual loss by using the reliable odometer measurements. Our system can also detect and solve the faulty information from wheel encoders to avoid the false estimate caused by wrong measurements. By carrying out the thorough experiments, we have demonstrated that our system can provide accurate, robust, and long-term localization for the wheeled robots moving on a plane.

In future work, we aim to exploit the line features to improve the performance of our algorithm in environments where only fewer point features are available. In addition, we will add the full IMU measurements to our system for improving the accuracy and dealing with the situation where both visual and wheel measurements cannot provide the valid measurements for localization.

ACKNOWLEDGMENT

We thank the author of [2] for providing a dataset to evaluate our algorithm in Section VI-A.

REFERENCES

[1] H. Lategahn, A. Geiger, and B. Kitt, "Visual SLAM for autonomous ground vehicles," in *Proc. IEEE Int. Conf. Robot. Automat.*, May 2011, pp. 1732–1737.

[2] K. J. Wu, C. X. Guo, G. Georgiou, and S. I. Roumeliotis, "Vins on wheels," in *Proc. IEEE Int. Conf. Robot. Automat.*, May 2017, pp. 5155–5162.

[3] A. I. Mourikis and S. I. Roumeliotis, "A multi-state constraint Kalman filter for vision-aided inertial navigation," in *Proc. IEEE Int. Conf. Robot. Autom.*, Apr. 2007, pp. 3565–3572.

[4] S. Leutenegger, S. Lynen, M. Bosse, R. Siegwart, and P. Furgale, "Keyframe-based visual-inertial odometry using nonlinear optimization," *Int. J. Robot. Res.*, vol. 34, no. 3, pp. 314–334, 2015.

[5] R. Mur-Artal and J. D. Tardós, "Visual-inertial monocular SLAM with map reuse," *IEEE Robot. Automat. Lett.*, vol. 2, no. 2, pp. 796–803, Apr. 2017.

[6] P. Li, T. Qin, B. Hu, F. Zhu, and S. Shen, "Monocular visual-inertial state estimation for mobile augmented reality," in *Proc. IEEE Int. Symp. Mixed Augmented Reality (ISMAR)*, Oct. 2017, pp. 11–21.

[7] J. Michot, A. Bartoli, and F. Gaspard, "Bi-objective bundle adjustment with application to multi-sensor slam," in *Proc. Int. Symp. 3D Data Process. Vis. Transmiss.*, 2010, pp. 1–8.

[8] A. Eudes, M. Lhuillier, S. Naudet-Collette, and M. Dhome, "Fast odometry integration in local bundle adjustment-based visual slam," in *Proc. 20th Int. Conf. Pattern Recognit.*, Aug. 2010, pp. 290–293.

[9] C. Forster, L. Carlone, F. Dellaert, and D. Scaramuzza, "IMU preintegration on manifold for efficient visual-inertial maximum-a-posteriori estimation," in *Proc. Robot., Sci. Syst.*, Rome, Italy, Jul. 2015.

[10] A. J. Davison, I. D. Reid, N. D. Molton, and O. Stasse, "MonoSLAM: Real-time single camera SLAM," *IEEE Trans. Pattern Anal. Mach. Intell.*, vol. 29, no. 6, pp. 1052–1067, Jun. 2007.

[11] G. P. Huang, A. I. Mourikis, and S. I. Roumeliotis, "A first-estimates jacobian EKF for improving SLAM consistency," in *Proc. Int. Symp. Exp. Robot.*, Athens, Greece, Jul. 2008, pp. 373–382.

[12] J. A. Hesch and S. I. Roumeliotis, "Consistency analysis and improvement for single-camera localization," in *Proc. IEEE Comput. Soc. Conf. Comput. Vis. Pattern Recognit. Workshops*, Jun. 2012, pp. 15–22.

[13] G. Klein and D. Murray, "Parallel tracking and mapping for small ar workspaces," in *Proc. 6th IEEE ACM Int. Symp. Mixed Augmented Reality (ISMAR)*, Nov. 2007, pp. 225–234.

[14] R. Mur-Artal, J. M. M. Montiel, and J. D. Tardós, "ORB-SLAM: A versatile and accurate monocular SLAM system," *IEEE Trans. Robot.*, vol. 31, no. 5, pp. 1147–1163, Oct. 2015.

[15] D. Galvez-López and J. D. Tardos, "Bags of binary words for fast place recognition in image sequences," *IEEE Trans. Robot.*, vol. 28, no. 5, pp. 1188–1197, Oct. 2012.

[16] H. Strasdat, J. M. M. Montiel, and A. J. Davison, "Scale drift-aware large scale monocular SLAM," in *Proc. Robot., Sci. Syst.*, Zaragoza, Spain, Jun. 2010.

[17] R. A. Newcombe, S. J. Lovegrove, and A. J. Davison, "DTAM: Dense tracking and mapping in real-time," in *Proc. IEEE Int. Conf. Comput. Vis.*, Nov. 2011, pp. 2320–2327.

[18] C. Forster, M. Pizzoli, and D. Scaramuzza, "SVO: Fast semi-direct monocular visual odometry," in *Proc. IEEE Int. Conf. Robot. Autom.*, Apr. 2014, pp. 15–22.

[19] J. Engel, T. Schöps, and D. Cremers, "LSD-SLAM: Large-scale direct monocular SLAM," in *Proc. Eur. Conf. Comput. Vis.*, Sep. 2014, pp. 834–849.

[20] J. Engel, V. Koltun, and D. Cremers, "Direct sparse odometry," *IEEE Trans. Pattern Anal. Mach. Intell.*, vol. 40, no. 3, pp. 611–625, Mar. 2016.

[21] R. Mur-Artal and J. D. Tards, "Probabilistic semi-dense mapping from highly accurate feature-based monocular SLAM," in *Proc. Robot., Sci. Syst.*, Rome, Italy, Jul. 2015.

[22] P. Pinies, T. Lupton, S. Sukkarieh, and J. D. Tardos, "Inertial aiding of inverse depth SLAM using a monocular camera," in *Proc. IEEE Int. Conf. Robot. Autom.*, Apr. 2007, pp. 2797–2802.

[23] M. Kleinert and S. Schleith, "Inertial aided monocular SLAM for GPS-denied navigation," in *Proc. IEEE Int. Conf. Multisensor Fusion Integr. Intell. Syst.*, Sep. 2010, pp. 20–25.

[24] E. Jones and S. Soatto, "Visual-inertial navigation, mapping and localization: A scalable real-time causal approach," *Int. J. Robot. Res.*, vol. 30, no. 4, pp. 407–430, 2011.

[25] M. Li and A. I. Mourikis, "High-precision, consistent EKF-based visual-inertial odometry," *Int. J. Robot. Res.*, vol. 32, no. 6, pp. 690–711, 2013.

[26] T. Qin, P. Li, and S. Shen, "VINS-mono: A robust and versatile monocular visual-inertial state estimator," *IEEE Trans. Robot.*, vol. 34, no. 4, pp. 1004–1020, Aug. 2018.

[27] J. Civera, O. G. Grasa, A. J. Davison, and J. M. M. Montiel, "1-Point RANSAC for extended Kalman filtering: Application to real-time structure from motion and visual odometry," *J. Field Robot.*, vol. 27, no. 5, pp. 609–631, 2010.

[28] D. Nistér, "An efficient solution to the five-point relative pose problem," *IEEE Trans. Pattern Anal. Mach. Intell.*, vol. 26, no. 6, pp. 756–770, Jun. 2004.

[29] V. Lepetit, F. Moreno-Noguer, and P. Fua, "EPnP: An accurate O(n) solution to the PnP problem," *Int. J. Comput. Vis.*, vol. 81, no. 2, pp. 155–166, 2009.

[30] B. K. P. Horn, "Closed-form solution of absolute orientation using unit quaternions," *J. Opt. Soc. Amer. A, Opt. Image Sci.,*, vol. 4, no. 4, pp. 629–642, 1987.

MEIXIANG QUAN received the B.S. degree in electronic information engineering from Harbin Engineering University, China, in 2014. She is currently pursuing the Ph.D. degree with the Multi-Agent Robot Research Center, Harbin Institute of Technology (HIT). Her research interests include visual SLAM, multi-sensor fusion, and semantic mapping.

SONGHAO PIAO received the Ph.D. degree from the Harbin Institute of Technology (HIT), in 2004. From 2006 to 2009, he held a Postdoctoral position in national key technology in robot technology and system at HIT. He is currently a Professor and a Doctoral Supervisor with the School of Computer Science and Technology, HIT. His research interests include robot intelligence control, pattern recognition, motion planning, and robot vision.

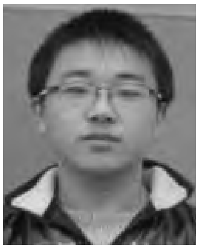

MINGLANG TAN received the B.S. degree in physics from Nanjing University, China, in 2014. He is currently a Researcher with Hyperception, Inc., Beijing. His primary research interests include visual SLAM and multi-sensor fusion.

SHI-SHENG HUANG received the Ph.D. degree in computer science from Tsinghua University, Beijing, in 2015. He is currently a Researcher and the CTO of a start-up company, Hyperception, Inc., Beijing. His primary research interests include the fields of computer graphics, computer vision, and visual SLAM.